Electrical and magnetic characterization of ultrathin films for magnetic sensors

Daniela Novo Jordão
Master in Engineering Physics
Department of Physics and Astronomy
Faculty of Sciences of the University of Porto
Faculty of Engineering of the University of Porto
2024

U.PORTO FC FACULDADE DE CIÊNCIAS UNIVERSIDADE DO PORTO

U.PORTO FEUP FACULDADE DE ENGENHARIA UNIVERSIDADE DO PORTO

MSc

Electrical and magnetic characterization of ultrathin films for magnetic sensors

Daniela Novo Jordão

Dissertation carried out as part of the Master in Engineering Physics

Department of Physics and Astronomy

2024

Supervisor
Dr. João Pedro Esteves de Araújo, Department of Physics and Astronomy, Faculty of Sciences, University of Porto

Co-supervisor
Dr. Diana Cristina Pinto Leitão, Department of Applied Physics, Eindhoven University of Technology

“ I think it’s a really good assignment (...) I’m really looking forward to writing it. ”

Katarina Stratford in *10 Things I Hate About You*

Acknowledgements

First, I would like to thank my supervisors, Dr. João Pedro and Dr. Diana, for their time and guidance. Thank you for giving me space to be wrong while pushing me to search for the right answer. Thank you for giving me every tool I needed to progress, for everything you've taught me and for the opportunity to be a part of your team.

To Mafalda Moreira, for being my PPMS guardian angel. Thank you for your time, help and knowledge.

To my parents. No amount of words can express the gratitude I feel for everything they've done for me throughout the years but, still, I will try. I want to thank them for always being present, even when they didn't have to, for always believing in me, much more than I ever did, for always pushing me to do better, to be better, and for teaching me the meaning of hard work and responsibility. Without their guidance and trust I wouldn't be the person I am today. I am forever grateful for all the sacrifices that they made so I could be here, writing this thesis. To my brother, for teaching me so much about perseverance, will-power and sacrifice at such a young age, and for always feeling like home. And to my grandparents, for their unconditional love, care and patience.

To all of my friends. To the ones that have been around since I was a little girl, who have seen me grow and never lost faith in my worth, to the ones with whom I shared the beautifully painful experience of taking a Physics or Engineering Physics degree with, and that have been my family when family is far, and to the ones that by chance entered my life and chose to stay and make it brighter, thank you all.

And finally, a special thank you to José Francisco, whom I am lucky enough to call both my colleague and friend. Thank you for everything that you've taught me throughout this year, for your patience, guidance and kindness, for every terribly amazing dad joke, and for all the advice during my caffeineless coffee breaks. I wouldn't have done it without you.

Resumo

Novos sensores baseados em torque de spin-órbita permitem detetar as três componentes do campo magnético num só elemento. Para melhorar e controlar a sua gama linear de deteção, é necessário uma caraterização magnética e elétrica dos dispositivos de filmes ultrafinos. Utilizando o SQUID MPMS®3, foi realizada uma caraterização magnética em três multicamadas de filmes ultrafinos: Ta (10) / CoFeB (1.2) / MgO (1.6) / Ta (20), Ta (5) / Ir (5) / CoFeB (1) / MgO (1.6) / Ta (20) e Ta (5) / Ir (5) / CoFeB (1.5) / MgO (1.6) / Ta (20), todas as espessuras em nanómetros. Valores de magnetização de saturação $M_S = (623 \pm 17)$ emu cm^{-3}, $M_S = (578 \pm 28)$ emu cm^{-3} e $M_S = (268 \pm 25)$ emu cm^{-3}, campo coercivo de $H_C = (9.7 \pm 0.6)$ Oe, $H_C = (10.5 \pm 0.6)$ Oe and $H_C = (11.0 \pm 0.6)$ Oe e campo de anisotropia de $H_K = (733 \pm 3)$ Oe, $H_K = (1328 \pm 10)$ Oe e $H_K = (112 \pm 4)$ Oe, respetivamente, foram obtidos. Em simultâneo, foi explorado o uso do PPMS® para desenvolver um protocolo para caraterização elétrica. As medidas foram realizadas num filme fino de a Ta (10) / CoFeB (1.2) / MgO (1.6) / Ta (20) padronizado numa estrutura de Hall, na qual a largura e o comprimento dos canais são 0.5 mm e 2.5 mm, respetivamente. Um coeficiente de Hall $R_H = (-1.034 \pm 0.005)\ \mu\Omega$ foi determinado. Assim, este trabalho confere protocolos dedicados a caraterizar as propriedades magnéticas e elétricas de filmes ultrafinos para deteção magnética.

Palavras-chave: Materiais, filmes ultrafinos, sensor magnético, magnetometria, medida elétrica

Abstract

Novel spin-orbit torque enabled sensors allow to detect the three components of the magnetic field in a single element. To improve and control their linear detection range, a magnetic and electrical characterization of the ultrathin film devices is required. Using the SQUID MPMS®3, magnetic characterization was performed on three multilayered ultrathin films: Ta (10) / CoFeB (1.2) / MgO (1.6) / Ta (20), Ta (5) / Ir (5) / CoFeB (1) / MgO (1.6) / Ta (20) and Ta (5) / Ir (5) / CoFeB (1.5) / MgO (1.6) / Ta (20), all thickness in nanometers. Values of saturation magnetization $M_S = (623 \pm 17)$ emu cm^{-3}, $M_S = (578 \pm 28)$ emu cm^{-3} and $M_S = (268 \pm 25)$ emu cm^{-3}, coercive field of $H_C = (9.7 \pm 0.6)$ Oe, $H_C = (10.5 \pm 0.6)$ Oe and $H_C = (11.0 \pm 0.6)$ Oe and anisotropy field of $H_K = (733 \pm 3)$ Oe, $H_K = (1328 \pm 10)$ Oe and $H_K = (112 \pm 4)$ Oe, respectively, were obtained. Simultaneously, the use of the PPMS® was explored to develop an electrical characterization protocol. The measurements were performed on a Ta (10) / CoFeB (1.2) / MgO (1.6) / Ta (20) thin film patterned into a Hall bar structure, in which the width and length of the channels are 0.5 mm and 2.5 mm, respectively. A Hall coefficient of $R_H = (-1.034 \pm 0.005)\ \mu\Omega$ was found. Thus, this work delivers protocols dedicated to characterize the magnetic and electric properties of ultrathin films for magnetic sensing.

Keywords: Materials, ultrathin films, magnetic sensor, magnetometry, electrical measurement

Table of Contents

List of Tables

List of Figures

1. Introduction

1.1. State of the art

Magnetic sensors play an important role in fields such as navigation, mechanical systems, biomedicine or industrial automation [1–5]. In current times, technology is demanding for ultracompact yet highly precise measurement systems. The miniaturization of either the active element or the readout electronics of a sensor is one important challenge [6]. Therefore, it is urgent to push the limits of magnetic sensing technologies and explore innovations in the materials design, processes and circuits.

A widely used solution to tackle the need for small and precise sensors are magnetoresistive sensors, which are thin-film solid-state devices that present spin-dependent resistance effects [7, 8]. Either based on anisotropic magnetoresistance [9], giant magnetoresistance [10] or tunnel magnetoresistance [11], these sensors are suitable for many applications due to their wide bandwith, high stability, high sensitivity and resolution, good linearity, all while maintaining a small size and low cost [12]. On the downside, each element allows for single-axis detection and in many technological applications, multiaxial detection is required [13].

Therefore, several techniques have been developed making use of the available sensors to measure the three components of the magnetic field. Either by using three magnetic sensors with their sensing directions along the three coordinate axes (x, y and z) [14] or planar sensors with an attached magnetic flux guide [15], it is indeed possible to detect the three components of the magnetic field. However, there are several downsides to these approaches as they are limited by the experimental set-up and environmental effects, which lead to non-orthogonality of the three sensing directions. This results in complicated adjustments of the subunits, low signal levels, high cross-sensitivities, numerous electrical connections, and the three magnetic field components not being measured at the same spot [4]. Therefore, to tackle these downsides, the need for a sensor capable of measuring the magnetic field vector using a single element arises.

An innovative solution to detect the three components of the magnetic field in a single element is by taking advantage of spin-orbit torque (SOT) [4, 5, 16].

On the basis of the proposed solution are multilayers of heavy metal (HM)/CoFeB/MgO [4, 5, 16, 17]. The ferromagnetic CoFeB layer provides the desired ferromagnetic behaviour and perpendicular magnetic anisotropy (PMA) and the HM layer allows for strong spin-orbit interaction [4, 5]. The combination of both these phenomena allows for external magnetic field sensitivity through the detection of the anomalous Hall effect as a function of the applied magnetic field [17, 18]. Due to spin-orbit torque, the hysteretic behaviour of the anomalous Hall resistance can be linearized and a linear response of anomalous Hall resistance with respect to magnetic field can be obtained [17, 18].

In 2021, Li et al. presented a Ta/CoFeB/MgO/Ta multilayer [4] that allowed magnetic field detection in a range of [-4,4] Oe in the z axis and [-10,10] Oe in the x and y axes. By exploiting spin-orbit interaction present in the Ta layer, they were able to detect magnetic field.

Following their work, in 2022, Guo et al. [5] switched the Ta layer for a W layer because it has a higher spin-orbit interaction and resulted in a range of detection of [-20,20] Oe in all directions, showing that through adequate thin-film engineering, such as material choice, it is possible to manipulate and optimize the detection range of spin-orbit torque-based sensors. In fact, by comparing both of these works, one can understand that the linear detection range is highly dependent on the HM layer because it dictates the charge-spin interconversion efficiency due to spin-orbit interaction.

A more recent report [19], from March 2024, has shown a linear range of [-300, 300] Oe acquired by having multiple repetitions of W/CoFeB/MgO heterostructures which increases anisotropy. Once again, it is shown that thin film engineering, here the optimization of the design, can greatly impact the detection range, translating into major advances in magnetic sensor development and opening a path for new studies on the topic.

1.2. Motivation and goals

Since spin-orbit torque enabled magnetic sensing is a novel technology, there are challenges to overcome to make them a competitive alternative. The main challenge is the control of the linear range of the sensors, which requires a robust understanding of both magnetic and electric properties of ultrathin films [16, 17].

The present work targets the design of an electric measurement protocol and the improvement of an established magnetic measurement protocol [20] to characterize ultrathin films for magnetic sensing, aiming for future development of spin-orbit torque enabled sensors like the ones reported in [4] and [5].

Additionally, a description of several theoretical principles underlying spin-orbit torque enabled sensing, followed by an explanation on magnetic anisotropies and their role in these sensors is provided with the intention of equipping the reader with some theoretical considerations to understand magnetic sensing enabled by spin-orbit torque.

Alongside the improvement of the magnetic measurements protocol it is intended to magnetically characterize HM/CoFeB/MgO/HM multilayers, exploring the influence of both the thickness of CoFeB and the addition of iridium in the magnetic properties of the device. Ir raised interest due to its larger atomic number compared to Ta and W. It is expected that a larger atomic number, which results in higher spin-orbit interaction, will allow to obtain a larger linear range and higher perpendicular magnetic anisotropy energy [21].

Lastly, considering the drive to develop a spin-orbit torque enabled magnetic sensor, a Hall cross microdevice is devised, based on the device reported in [4].

The developed work took place at the Institute of Physics for Advanced Materials, Nanotechnology and Photonics (IFIMUP) which develops multidisciplinary scientific activity in the fields of pure and applied physics. The present work is integrated in the Multifunctional Magnetic Materials research group as an emerging research topic that started in late 2022. It is important to highlight that all depositions were made possible by Dr. Diana Leitão in the Department of Applied Physics at Eindhoven University of Technology, and in order to magnetically and electrically characterize the samples the SQUID Magnetometer (MPMS®3) and PPMS® existing at IFIMUP were employed.

2. Theoretical framework

In this chapter, a theoretical framework is presented, in order to equip the reader with the necessary tools to understand the principles of operation underlying spin-orbit torque enabled magnetic field sensors. At first, general discussions on each topic are provided, finishing with a description on how each phenomenon can be exploited into magnetic field sensing.

2.1. Stoner-Wohlfarth model

The Stoner-Wohlfarth model [22] presents a framework to explain magnetic hysteresis arising from coherent rotation of the magnetization. This is a single domain model, meaning that the possible different domains of the ferromagnet are not considered. The ferromagnet is assumed to have uniaxial magnetic anisotropy and its magnetization rotates with the variation of magnetic field, H_a, but it is restricted to the plane containing both the magnetic field and the anisotropy axis. In this way, the problem becomes two-dimensional and the changes in magnetization can be represented only by an angle. According to this model, magnetization dynamics is determined by minimizing the energy of the ferromagnetic system for the given magnetic field. Therefore, all the energy terms involved in the system will have a contribution to its magnetic behaviour.

2.1.1 Zeeman energy

When an external magnetic field, $\boldsymbol{H}_a$, is applied to a ferromagnetic material with magnetization $\boldsymbol{M}$, dipolar magnetic interaction gives rise to a potential energy called the Zeeman energy [23],

$$\varepsilon_z = -\mu_0 \boldsymbol{M} \cdot \boldsymbol{H}_a = -\mu_0 M H \cos\phi \tag{2.1}$$

where ϕ is the angle between the magnetization and the external magnetic field.

This energy density term is said to be unidirectional as it only reaches a minimum when $\phi = 2\pi n$, for any integer n, meaning that the Zeeman energy is responsible for aligning the magnetization parallel to the external magnetic field.

2.1.2 Anisotropy

Most ferromagnetic materials are known to have magnetic anisotropy, meaning that there is a preferential direction to align their spontaneous magnetization along one or more easy axes [6]. There are several sources of anisotropy. In thin films the main anisotropy contributions are shape and surface effects.

2.1.2.1 Shape anisotropy

When a magnetic field is applied to a sample, another magnetic field arises inside the sample as a response, in opposite direction to the magnetization [6, 23]. This field is known as demagnetizing field, $\boldsymbol{H}_d$, and it greatly depends on the shape of the sample. Under certain approximating conditions, inside the ferromagnet the demagnetizing field is uniform and proportional to the magnetization [6, 23],

$$\boldsymbol{H}_d = -\mathcal{N}_d \boldsymbol{M} \tag{2.2}$$

where $\mathcal{N}_d$ is the demagnetizing tensor.

Considering a thin film lying on the xOy plane, and assuming the dimensions in x and y are infinite and the demagnetizing factors $\mathcal{N}_x$ and $\mathcal{N}_y$ are zero and the only non-null component in the tensor is N_d^{zz} = 1.

$$\begin{pmatrix} \boldsymbol{H}_d^x \\ \boldsymbol{H}_d^y \\ \boldsymbol{H}_d^z \end{pmatrix} = -\begin{pmatrix} 0 & 0 & 0 \\ 0 & 0 & 0 \\ 0 & 0 & N_d^{zz} \end{pmatrix} \begin{pmatrix} \boldsymbol{M}_x \\ \boldsymbol{M}_y \\ \boldsymbol{M}_z \end{pmatrix} = -\begin{pmatrix} 0 & 0 & 0 \\ 0 & 0 & 0 \\ 0 & 0 & 1 \end{pmatrix} \begin{pmatrix} \boldsymbol{M}_x \\ \boldsymbol{M}_y \\ \boldsymbol{M}_z \end{pmatrix} = \begin{pmatrix} 0 \\ 0 \\ -M_z \end{pmatrix} \tag{2.3}$$

The energy density due to the demagnetizing field stored in a material magnetized to saturation, $\boldsymbol{M}_s$, is given by [6, 23]

$$\varepsilon_d = -\mu_0 \int_0^{\boldsymbol{M}_s} \boldsymbol{H}_d \cdot d\boldsymbol{M} \tag{2.4}$$

In this particular case, the energy density due to the demagnetizing field stored in a thin film lying on the xOy plane and magnetized to saturation becomes

$$\varepsilon_d = \frac{\mu_0}{2} M_{sz}^2 = \frac{\mu_0}{2} M_s^2 \cos^2\theta \tag{2.5}$$

where θ is the angle between the magnetization direction and the surface normal.

From equation 2.5 it is clear that the energy reaches a minimum when $\theta = \frac{\pi}{2} + n\pi$, for any integer n, showing that the demagnetizing field wants to align the magnetization in-plane. This energy term is uniaxial, meaning that the minimum is reached regardless of the magnetization direction being parallel (positive) or antiparallel (negative) to the surface normal. Thus, it is possible to conclude that the demagnetizing field gives rise to a shape anisotropy, leading to a preferential alignment of the magnetization which directly depends on the shape of the sample.

2.1.2.2 Surface anisotropy

In thin films, there is a kind of anisotropy that comes from the surface, called surface anisotropy [6]. Mainly, it arises from the coupling of the surface atoms to the crystal field produced by their surroundings. Although it originates in the surface monolayer that has broken symmetry, this anisotropy can extend to the first few monolayers [6]. Therefore, it is possible to describe the surface anisotropy of a thin film as a sum of terms that scale with volume, K_V, and surface area, K_S, turning the effective anisotropy constant K_{eff} into

$$K_{\text{eff}} = K_V + \frac{K_S}{t} \tag{2.6}$$

where t is the film thickness [6].

The energy density associated with surface anisotropy is given by

$$\varepsilon_s = K_{\text{eff}} \sin^2\theta \tag{2.7}$$

where θ is the angle between the magnetization and the surface normal [6].

Surface anisotropy is particularly interesting as it can give different preferential directions depending on the thickness of the sample. To minimize equation 2.7 there are two possible cases: $K_{\text{eff}} < 0$ and $K_{\text{eff}} > 0$. In the first case, when $K_{\text{eff}} < 0$, the energy reaches its minimum for $\theta = \frac{\pi}{2} + n\pi$, for any integer n, and the magnetization wants to align in-plane. In the second case, when $K_{\text{eff}} > 0$, the energy reaches its minimum value when $\theta = n\pi$, for any integer n, and the magnetization wants to align perpendicularly to the surface, in the out-of-plane direction. This anisotropy term is also uniaxial.

Given the fact that both K_V and K_S only depend on the material of the sample, not on its size or thickness [6], it is clear that, for a certain sample, a change in thickness can result in a transition from a state with in-plane anisotropy to a state with out-of-plane anisotropy (and vice-versa). Particularly, a sample with a negative value of K_V and a positive value of K_S, will have PMA until a thickness of $t = -\frac{K_S}{K_V}$ is reached. When $t > -\frac{K_S}{K_V}$, the energy density term becomes negative and the sample shows in-plane anisotropy.

Thus, the magnetic anisotropy of a sample is given by the sum of each anisotropic contribution (shape and surface). In order to control the anisotropy of a certain ferromagnetic thin film, not only the composing material, but also the shape and thickness of the thin film, are fundamental characteristics.

2.1.3 Magnetization dynamics

Magnetization dynamics is highly dependent on magnetic anisotropy. As seen before, anisotropy arises as a result of energy minimization, meaning that for a ferromagnet with PMA, the energy is minimized when the magnetization points perpendicular to the sample. Therefore, different behaviours are expected when a magnetic field is applied along the easy or hard axes. [6]

First, consider the case where a ferromagnetic material is subject to an external magnetic field along its easy axis: a ferromagnet with PMA subject to a magnetic field H_z ($\alpha = 0°$). Due to PMA, there are two energy minima: when the magnetization, M_s, points up or down in the z axis, separated by an energy barrier. Considering that the ferromagnet is in a state with a spontaneous magnetization $+M_s$, when a magnetic field is applied in $-z$, the system's energy starts to increase, decreasing the energy barrier between the two minima. When the magnetic field reaches the value of the coercive field, the energy barrier vanishes and the state $+M_s$ is no longer an energy minimum. Therefore, magnetization switches to $-M_s$.

An analogous behaviour is observed if a magnetic field in $+z$ is applied to a state $-M_s$. From this description, it is straightforward that when a ferromagnetic material is subject to a magnetic field along its easy-axis, the magnetization can switch between two values, $+M_s$ or $-M_s$, leading to an hysteresis loop with coercivity. In this case, the dominant magnetization switching process is domain nucleation.

On the other hand, we now consider a ferromagnetic material with a magnetic field applied along a hard-axis: a ferromagnet with PMA subject to a magnetic field H_x ($\alpha = 90°$). In this scenario, the magnetic field is not pointing in an energy minimization direction.

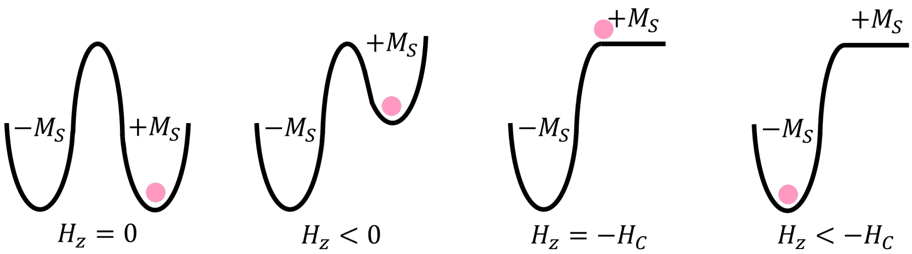

Figure 2.1: Energy valley scheme to describe magnetization switching when a magnetic field is applied along the easy axis.

Therefore, the spins will suffer coherent rotation and start to align with the magnetic field, achieving a magnetization component in x. This component increases linearly with the magnetic field module, as the z component decreases. Once the magnetic field equals the anisotropy field, the sample becomes fully magnetized in x and a saturation magnetization is achieved.

For intermediate angles between the applied magnetic field and the anisotropy axis of the sample, ($\alpha \in]0, 90[^\circ$), the magnetic behaviour is a combination of both scenarios, where the coercivity is given by nucleation of magnetic domains while the slope is a consequence of coherent rotation of spins. Figure 2.2 represents the magnetization curves for several values of α [6].

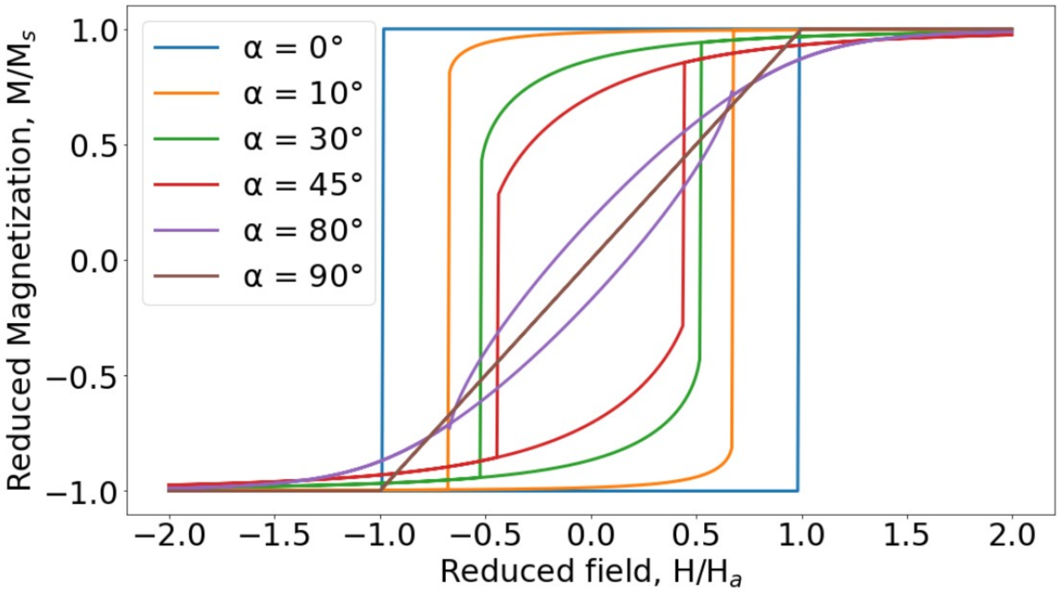

Figure 2.2: Magnetization curves for the Stoner-Wohlfarth model for various angles α between the field direction and easy axis. H is given in units of the anisotropy field H_a

2.2. Understanding spin-orbit coupling based phenomena for magnetic sensing

2.2.1 Spin-orbit interaction

Consider the Bohr atomic model [24], where an electron orbits a nucleus with a velocity v. The protons in the nucleus generate an electric field, $\boldsymbol{E}$, that interacts with the electron leading it to acquire a centripetal acceleration, $\boldsymbol{a}$, that keeps it in a well-defined orbit of radius r.

$$\boldsymbol{E} = \frac{Ze}{4\pi\epsilon_0}\frac{\boldsymbol{r}}{r^3} \tag{2.8}$$

$$\boldsymbol{a} = -\frac{e}{m_e}\boldsymbol{E} \tag{2.9}$$

Z stands for the atomic number, e for the elementary charge, ϵ_0 for the vacuum permittivity and m_e for the mass of the electron.

If we consider the electron reference frame, the electron is at rest, and the nucleus, which has a positive charge, is orbiting the electron. The movement of positive charge is responsible for generating a current which results in the generation of a magnetic field. To determine the magnetic field in the electron reference frame, $\mathscr{B}$, one needs to resort to Lorentz transformations, considering both electric and magnetic fields in the lab reference frame, $\boldsymbol{E}$ and $\boldsymbol{B}$, respectively, and the Lorentz factor $\gamma = \left(1 - \left(\frac{v}{c}\right)^2\right)^{-\frac{1}{2}}$ [25].

$$\mathscr{B} = \gamma\left(\boldsymbol{B} - \frac{\boldsymbol{v} \times \boldsymbol{E}}{c^2}\right) \tag{2.10}$$

Taking into account that the electron has a magnetic dipole moment $\boldsymbol{\mu}$ [6],

$$\boldsymbol{\mu} = -g_s\frac{\mu_B}{\hbar}\boldsymbol{S} \tag{2.11}$$

where g_s is the g-factor of the electron's spin, μ_B is the Bohr magneton, $\hbar$ is the reduced Planck constant and $\boldsymbol{S}$ is the spin vector operator, one can expect the magnetic field $\mathscr{B}$ to produce a torque in said magnetic dipole. The torque is given by [25]

$$\frac{d\boldsymbol{S}}{dt} = \boldsymbol{\mu} \times \mathscr{B} = -g_s\frac{\mu_B}{\hbar}\boldsymbol{S} \times \mathscr{B} \tag{2.12}$$

At first instance, expression 2.12 seems correct. However, it lacks an important correction. As seen before, in the lab reference frame, the electron is accelerated, making the electron reference frame non-inertial. In reality, the electron reference frame is moving with an angular velocity ω, and so, the change in spin with respect to time has to take this rotation into account, becoming [25]

$$\frac{d\boldsymbol{S}}{dt} = -g_s \frac{\mu_B}{\hbar} \boldsymbol{S} \times \mathscr{B} - \boldsymbol{S} \times \boldsymbol{\omega} \tag{2.13}$$

It is now possible to define a magnetic effective field, $\mathscr{B}_{\mathscr{L}}$, so that

$$\frac{d\boldsymbol{S}}{dt} = -g_s \frac{\mu_B}{\hbar} \boldsymbol{S} \times \left(\mathscr{B} + \frac{\hbar}{g_s \mu_B} \boldsymbol{\omega} \right) = -g_s \frac{\mu_B}{\hbar} \boldsymbol{S} \times \mathscr{B}_{\mathscr{L}} \tag{2.14}$$

The Hamiltonian of this interaction is given by

$$H_{SO} = -\boldsymbol{\mu} \cdot \mathscr{B}_{\mathscr{L}} \tag{2.15}$$

which becomes

$$H_{SO} = g_s \frac{\mu_B}{\hbar} \boldsymbol{S} \cdot \left(\mathscr{B} + \frac{\hbar}{g_s \mu_B} \boldsymbol{\omega} \right) \tag{2.16}$$

Through Lorentz transformations it is possible to show that ω depends on the velocity and acceleration of the electron in the lab reference frame, $\omega = \frac{\gamma^2}{\gamma+1} \frac{\boldsymbol{a} \times \boldsymbol{v}}{c^2} = \frac{1}{2} \frac{\boldsymbol{a} \times \boldsymbol{v}}{c^2}$, considering that $v << c$, $\gamma \sim 1$. The obtained $\frac{1}{2}$ factor is the famous Thomas precession factor [20, 25].

By expressing the velocity of the electron in terms of its linear momentum, $\boldsymbol{v} = \frac{\boldsymbol{p}}{m_e}$, substituting both the acceleration, $\boldsymbol{a}$, and the electric field, $\boldsymbol{E}$, by equations 2.9 and 2.8, respectively, and considering that there is no external magnetic field in the lab reference frame, $\boldsymbol{B} = 0$, it is possible to obtain the Hamiltonian of the spin-orbit interaction as a function of the atomic number.

$$H_{SO} = \frac{Ze^2}{8\pi\epsilon_0 {m_e}^2 c^2 r^3} \boldsymbol{S} \cdot (\boldsymbol{r} \times \boldsymbol{p}) \tag{2.17}$$

Finally, defining the orbital momentum as $\boldsymbol{L} = \boldsymbol{r} \times \boldsymbol{p}$, the spin-orbit interaction Hamiltonian is given by

$$H_{SO} = \frac{Ze^2}{8\pi\epsilon_0 {m_e}^2 c^2 r^3} \boldsymbol{S} \cdot \boldsymbol{L} \tag{2.18}$$

The analysis of expression 2.18 allows us to assert that the electron's orbital motion couples its spin angular momentum with its orbital angular momentum, meaning that changes in electron spin greatly affect its motion through a material. Although almost irrelevant in most cases, this energy term can become quite significant, making it crucial to determine its occurrence conditions. If we consider that the value of $\langle \frac{1}{r^3} \rangle \propto Z^3$, then we can state that $\langle H_{SO} \rangle \propto Z^4$. In other words, the spin-orbit interaction becomes more significant in elements with a higher atomic number, where electron-nucleus interactions are stronger. This observation is extremely important for the development of sensors based on spin-orbit interactions, as it demonstrates that by correctly selecting the element used to fabricate the sensor, it is possible to significantly enhance this effect.

Several interesting phenomena can emerge from spin-orbit interaction [26] leading to new interactions and electronic states. From spin-splitting of electronic bands, to the emergence of topological materials, to charge-spin interconversion and new transport phenomena, spin-orbit coupling provides a whole new range of phenomena that is fundamental for spintronic applications.

2.2.2 Magnetization switching

2.2.2.1 Spin-Hall effect

The spin-Hall effect (SHE) is a phenomenon that generates a pure spin-current from a spin-neutral charge current flowing in a material with high spin-orbit coupling [16, 17]. To better understand this effect, let us consider a single layer heavy metal with no inversion symmetry that exhibits high spin-orbit coupling. Now, we consider a charge current consisting of both spin-up and spin-down electrons in equal amount so that the charge current is spin-neutral. As the spin-neutral charge current flows through the heavy metal layer, the spin-up and spin-down electrons will be deflected in opposite directions as a result of spin-dependent scattering events [16]. The deflection of spin-up and spin-down electrons in opposite directions generates a transverse spin current in the heavy metal. Due to the equilibrium of charge in each side of the layer, no Hall resistance arises. This phenomenon is represented in figure 2.3.

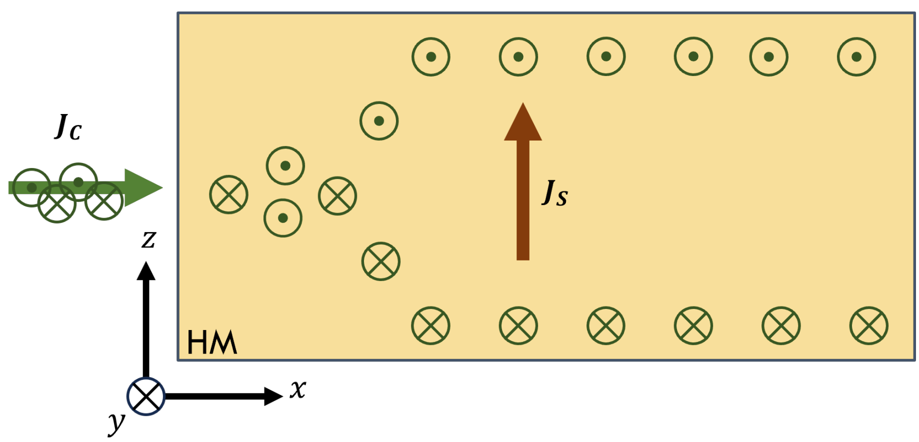

Figure 2.3: Representation of spin-Hall effect in a heavy metal layer. The injected charge current, J_C, and the generated spin current, J_S, are represent by green and red arrows, respectively. ⊗ and ⊙ represent the spin polarization direction.

Equation 2.19 describes the spin-Hall effect, where, $\boldsymbol{J_C}$ is the applied spin-neutral charge current density, $\boldsymbol{J_S}$ is the generated spin current density, $\boldsymbol{\sigma}$ is the polarization of the spin current and Θ_{SH} corresponds to a coefficient that scales the intensity of the effect and corresponds to the so-called spin-Hall angle. In this way, the spin-Hall angle is an intrinsic property of the material and is related to the charge-spin conversion efficiency [17].

$$\boldsymbol{J_S} = \frac{\hbar}{2e}\Theta_{SH}\left(\boldsymbol{\sigma} \times \boldsymbol{J_C}\right) \tag{2.19}$$

2.2.2.2 Landau-Lifshitz-Gilbert equation and spin-orbit torque

Considering now a heavy metal/ferromagnet interface, where spin-Hall effect occurs in the heavy metal, new phenomena arises, namely, the spin-orbit torque.

Due to spin-Hall effect in the heavy metal, the deflection of electrons in opposite directions results in spin accumulation at the interface between the heavy metal and ferromagnet. These spins can diffuse into the ferromagnetic layer and exert a torque on its magnetization [17].

The Landau-Lifshitz-Gilbert equation (LLG) (equation 2.20) provides a phenomenological description of magnetization dynamics [27].

$$\frac{d\boldsymbol{m}}{dt} = -\gamma'\boldsymbol{m} \times \boldsymbol{H}_{\text{eff}} + \lambda\boldsymbol{m} \times \left(\boldsymbol{H}_{\text{eff}} \times \boldsymbol{m}\right) \tag{2.20}$$

γ' and λ represent precessional and damping parameters, respectively, $\boldsymbol{m}$ the magnetization versor and $\boldsymbol{H}_{\text{eff}}$ the effective magnetic field.

This equation represents two types of torques: the field-like torque is given by the effective magnetic field and causes the magnetization to precess around the direction of the given field, the damping-like torque is perpendicular to the field-like torque and tries to align the magnetization with the effective field direction [17]. It is clear that the effective field controls the dynamics of the magnetization, therefore, it needs to take into account all the interactions with the magnetization. We can isolate the SOT contribution and represent the effective field as the sum of field generated by SOT, $\boldsymbol{H}_{\text{SOT}}$, and the field generated by the remaining contributions, $\boldsymbol{H}'_{\text{eff}}$.

$$\frac{d\boldsymbol{m}}{dt} = -\gamma'\boldsymbol{m} \times \boldsymbol{H}'_{\text{eff}} + \lambda\boldsymbol{m} \times \left(\boldsymbol{H}'_{\text{eff}} \times \boldsymbol{m}\right) - \gamma'\boldsymbol{m} \times \boldsymbol{H}_{\text{SOT}} + \lambda\boldsymbol{m} \times \left(\boldsymbol{H}_{\text{SOT}} \times \boldsymbol{m}\right) \tag{2.21}$$

Therefore, it's possible to define the spin-orbit torque as

$$\boldsymbol{\tau}_{\text{SOT}} = -\gamma' \boldsymbol{m} \times \boldsymbol{H}_{\text{SOT}} + \lambda \boldsymbol{m} \times (\boldsymbol{H}_{\text{SOT}} \times \boldsymbol{m}) \tag{2.22}$$

Considering $\boldsymbol{H}_{\text{SOT}} = a_j(\boldsymbol{m} \times \boldsymbol{\sigma} + \xi \boldsymbol{\sigma})$, where $\boldsymbol{\sigma}$ is the spin current polarization direction, and $\xi = \frac{b_J}{a_J}$ where a_J and b_J represent the magnitude of the damping-like and field-like contribution, respectively, the spin-orbit torque can be defined as

$$\boldsymbol{\tau}_{\text{SOT}} = \frac{\gamma'}{1+\lambda^2} a_J((1+\lambda\xi)\boldsymbol{m} \times (\boldsymbol{\sigma} \times \boldsymbol{m}) + (a - \xi)\boldsymbol{\sigma} \times \boldsymbol{m}) \tag{2.23}$$

The term of the form $\boldsymbol{m} \times (\boldsymbol{\sigma} \times \boldsymbol{m})$ represents the damping-like torque, $\boldsymbol{\tau}_{\text{DL}}$, and the term of the form $\boldsymbol{\sigma} \times \boldsymbol{m}$ represents the field-like torque, $\boldsymbol{\tau}_{\text{FL}}$.

Even though both are significant for magnetization switching, it is important to distinguish their roles. While the damping-like torque is responsible for effectively switching magnetization, dictating the switching direction, the field-like torque is related to the speed of the switching process as well as the required critical switching current [28, 29].

2.3. Basics of anomalous Hall effect

Hall effect experiments on ferromagnetic materials led to the discovery of a new charge transport phenomenon: the anomalous Hall effect [18].

In non-magnetic materials, the Hall resistivity scales linearly with applied magnetic field. Distinctly, it was found that in ferromagnets the Hall resistivity greatly increases and then stabilizes at a certain value, as seen in figure 2.4. Thus, there must be an anomalous contribution to the Hall resistivity of ferromagnets which does not depend on the external field [6]. Decades after this discovery, Smith [30] and Pugh [31, 32] independently proposed an empirical relation between magnetization and Hall resistivity.

$$\rho_{xy} = R_0 H_z + R_1 M_z \tag{2.24}$$

R_0 and R_1 represent the ordinary and anomalous Hall coefficients, respectively. The first term on the right side of the equation, which is dependent on the external magnetic field, corresponds to the ordinary Hall effect contribution, as seen in non-magnetic materials. This term scales linearly with applied magnetic field. The second term, proportional to the magnetization, translates the anomalous Hall effect. In ferromagnetic materials, the anomalous Hall effect has been shown to be much greater than the ordinary Hall effect, hence the anomalous Hall coefficient of the material must be significantly larger than its ordinary Hall coefficient, $R_1 >> R_0$ [33]. Therefore, the Hall resistivity of a ferromagnetic material can be considered proportional do the magnetization.

$$\rho_{xy} \sim R_1 M_z \tag{2.25}$$

Three distinct contributions yield the anomalous Hall effect: intrinsic, skew-scattering and side-jump contributions [18]. The intrinsic contribution depends only on the band structure of the crystal, hence its designation. Due to the band-structure and spin-orbit coupling a transverse velocity arises in between scattering events, leading to different spin polarization in different directions [18]. Skew-scattering occurs when an electron scatters due to an impurity or phonon [34]. In this case, the spin-orbit coupling gives an effective field gradient along the scattering vector and the scattering becomes spin dependent. Lastly, side-jump corresponds to an accumulation of spin at the lateral boundaries of the sample as a result of an effective field gradient originated by spin-orbit coupling. In fact, there is an effective field gradient along the incoming and outcoming directions, which upon repeated scattering events leads to said accumulation [33].

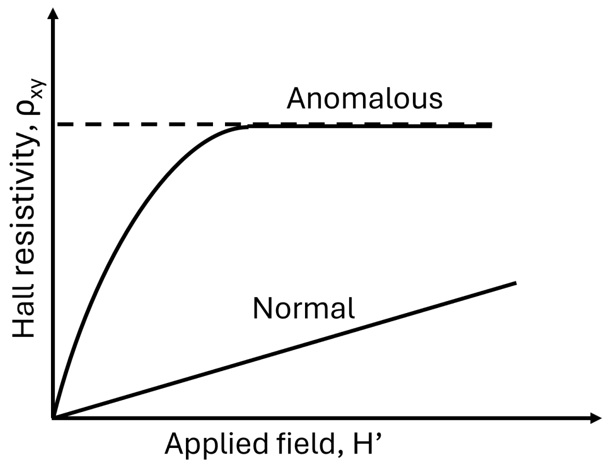

Figure 2.4: Variation of Hall resistivity with applied magnetic field with (Anomalous) and without (Normal) the anomalous Hall effect contribution.

2.4. Principles of sensing operation

Consider a Hall cross structure based upon HM/FM/MgO heterostructures that exhibits PMA, and a charge current being injected into the device in the x direction. The charge current density is given by $\boldsymbol{J}_x$.

The first thing to note is the fact that the current travelling through the heavy metal generates a magnetic field. This field, known as the Oersted field, $\boldsymbol{B}^{\mathrm{Oe}}$, follows the right-hand rule and thus has components in both the y and z directions, as shown in figure 2.5b [35]. Since the ferromagnet has PMA and a relatively small coercive field, small values of B_z^{Oe} can saturate its magnetization. However, on one side of the sample, B_z^{Oe} points up ($+z$), while on the other B_z^{Oe} points down ($-z$). Therefore, a domain wall arises at the center of the Hall cross separating two domains with symmetrical magnetization [35]. At this point, both the device magnetization and anomalous Hall resistance (proportional to M_z) are equal to zero, $M_z = 0$, $R_H \sim 0\,\Omega$.

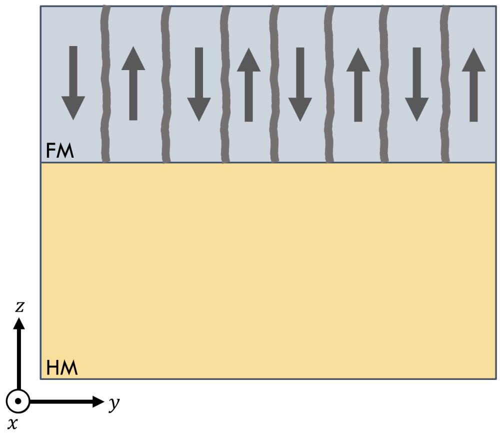

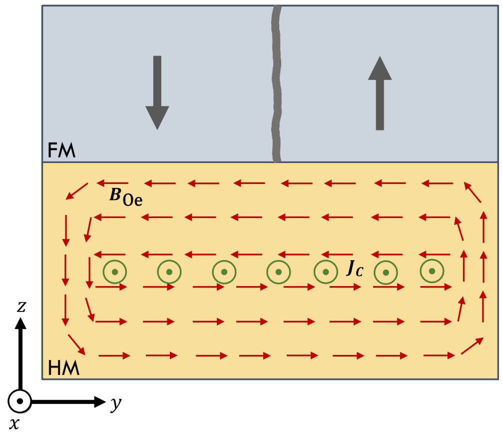

Figure 2.5: Configuration of the ferromagnetic domains in the ferromagnet (FM) in the absence (a) or presence (b) of Oersted field, $\boldsymbol{B}^{\mathrm{Oe}}$, inside the heavy metal (HM) layer. Magnetization of the domains represented by grey arrows, $\boldsymbol{B}^{\mathrm{Oe}}$ represented in red arrows and charge current, $\boldsymbol{J}_C$, represented by green $\odot$.

Simultaneously, the current in the HM gives origin to the spin-Hall effect. Figure 2.6 shows that a charge current in x generates a spin current in z polarized in y. Therefore, there is spin accumulation at the HM/FM interface. As these spins diffuse through the FM layer, they exert a torque in its magnetization which is governed by $\boldsymbol{H}_{\mathrm{SOT}}$. In this case, $\boldsymbol{H}_{\mathrm{SOT}}$ depends on the spin polarization, $\boldsymbol{\sigma}_y$, and on the magnetization within the domain wall, $\boldsymbol{m}$. $\boldsymbol{H}^{\mathrm{SOT}}$ can be rewritten as

$$\boldsymbol{H}^{\mathrm{SOT}} \propto (\boldsymbol{z} \times \boldsymbol{J}_x) \times \boldsymbol{m} \tag{2.26}$$

which leads to [36]

$$H_z^{\text{SOT}} = \frac{\hbar}{2eM_s t}\Theta_{SH} J_{x(y)} m_{x(y)} \tag{2.27}$$

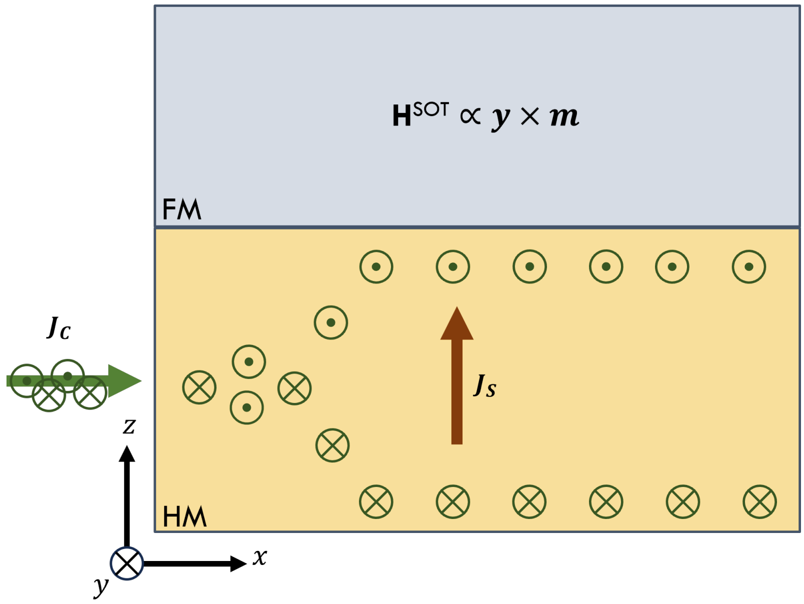

Figure 2.6: Representation of spin-Hall effect in a HM/FM bilayer. The injected charge current, J_C, and the generated spin current, J_S, are represent by green and red arrows, respectively. ⊗ and ⊙ represent the spin polarization direction.

From equation 2.27 is clear that an in-plane external magnetic field can drive domain wall propagation. The in-plane field orients the magnetization within the domain wall to achieve an in-plane component $m_{x(y)}$. If $m_{x(y)}$ is collinear with $J_{x(y)}$, domain wall motion occurs [4]. Domain wall motion is accompanied by a change in M_z and thus a change in R_H. Hence, when a current is applied along the x axis, both H_x and H_z can drive domain wall motion and origin an anomalous Hall resistance. H_y, however, cannot due to the lack of SOT resulting from its perpendicularity to the current [4]. Similarly, when a current density J_y is applied, both H_y and H_z can drive domain wall motion and H_x cannot.

Figure 2.7 shows a schematic of domain wall motion under H_x, H_y and H_z when J_x (2.7a) or J_y (2.7b) is applied.

Furthermore, when a 3D magnetic field $\boldsymbol{H} = (H_x, H_y, H_z)$ and an in-plane current are applied to the device, the resulting domain wall displacement is modulated by a combination of in-plane and out-of-plane fields [4, 5]. For the case where domain wall motion is driven by an in-plane field, the direction of H_z^{SOT} depends on the relative directions of both the in-plane current and in-plane component of the magnetization (equation 2.27). When the current direction reverses, the domain wall motion reverses [4, 5]. For the case where domain wall motion is driven by an out-of-plane field, the direction of domain wall motion depends only on the direction of H_z. This contrasting behaviour allows to separate the contributions of in-plane and out-of-plane fields, allowing for the detection of both [4, 5]. To separate these contributions an analysis of the magnetic hysteresis loops in each case is required.

The existence of two magnetic domains with symmetrical magnetization separated by a domain wall located at the center of the Hall cross results in the loss of coercivity in the magnetic hysteresis loop of the device [4, 5]. In this particular case, an out-of-plane magnetic field results in coherent rotation of spins within the domain wall increasing the size of the magnetic domain positively/negatively magnetized. This is seen as the domain wall linearly moving along the sample. Therefore, a linear response of M_z to H_z is observed, reaching saturation values when the field is high enough to fully rotate all spins.

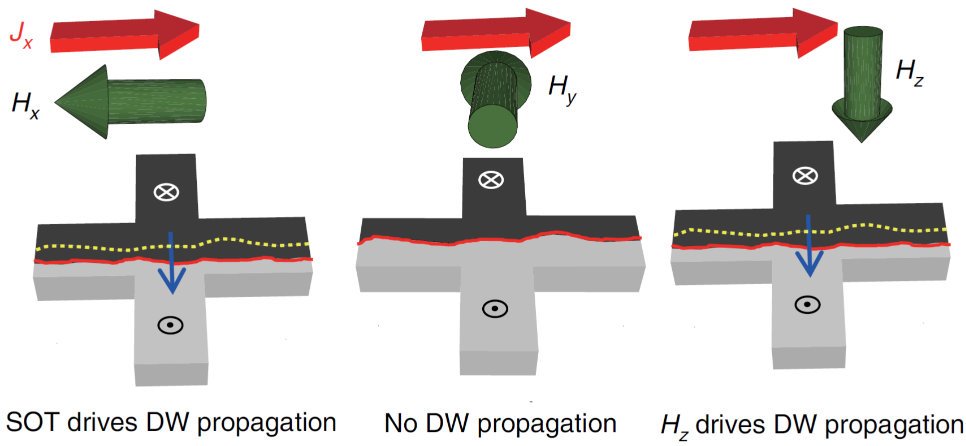

(a) Schematic of domain wall motion under H_x, H_y and H_z when J_x is applied.

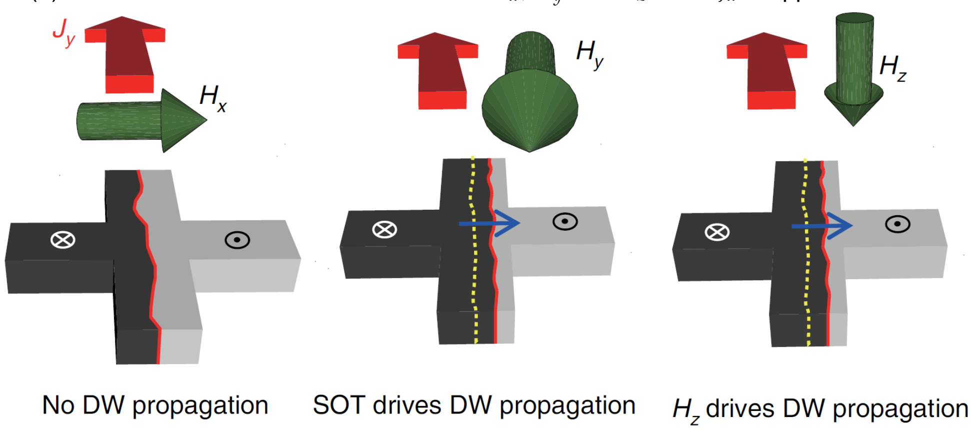

(b) Schematic of domain wall motion under H_x, H_y and H_z when J_y is applied.

Figure 2.7: Schematic of domain wall motion under H_x, H_y and H_z when in-plane current is applied. The yellow dotted line shows the initial position of the domain wall and the red solid line represents its final position. The blue arrow indicates the direction of domain wall motion. Reproduced with permission from [4].

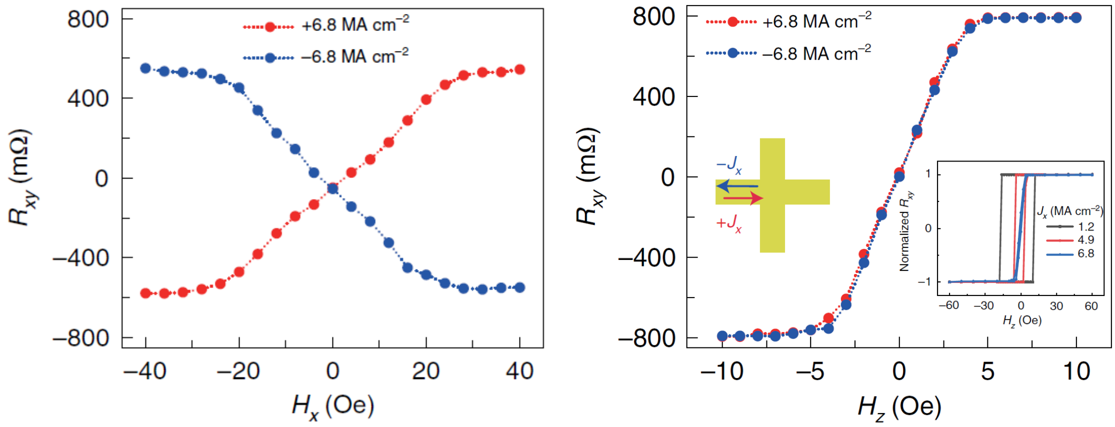

(a) R_{xy} as a function of H_x.

(b) R_{xy} as a function of H_z

Figure 2.8: R-H curves under ± 6.8MA cm^{-2} (curves obtained with negative current in blue and with positive current in red). Reproduced with permission from [4].

In turn, an in-plane field (i.e. H_x) parallel to the applied charge current (i.e. J_x), results in a positive perpendicular magnetic field, and the resulting hysteresis loop behaves similarly to the $R_{xy} - H_z$ curve. Finally, an in-plane field antiparallel (i.e. $-H_x$) to the applied charge current (i.e. J_x), results in a negative perpendicular magnetic field, and the resulting hysteresis loop behaves symmetrically to the $R_{xy} - H_x$ curve. The three scenarios are represented in figure 2.8 (recall that M_z is proportional to R_{xy}).

By exploiting the symmetry in the $R_{xy} - H_x$ curves under different current polarities, it's possible to isolate the net resistance contributed by H_z from the net resistance contributed by H_x [4].

$$R(H_x) = \frac{R_{xy}(+J_x) - R_{xy}(-J_x)}{2} \tag{2.28}$$

$$R(H_z) = \frac{R_{xy}(+J_x) + R_{xy}(-J_x)}{2} \tag{2.29}$$

Analogous results are obtained for H_z and H_y for a current along the y axis.

3. Magnetic characterization

3.1. Sample characteristics

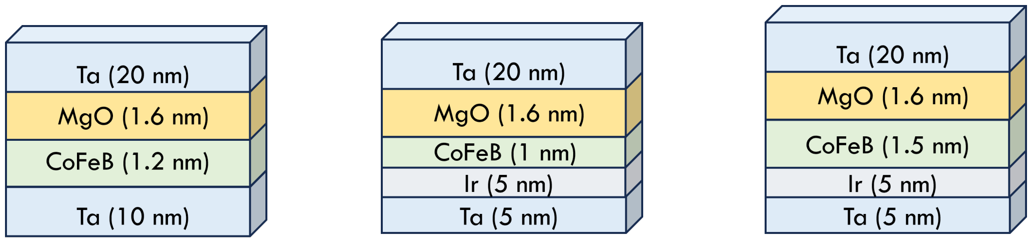

(a) CF1. (b) CF2. (c) CF3.

Figure 3.1: Schematic of the continuous films under study.

In this work, the magnetic properties of three multilayer samples were studied: CF (continuous film) 1, 2 and 3. A schematic of each is represented in figure 3.1.

The CF1 sample consists of a Ta (10) / $Co_{60}Fe_{20}B_{20}$ (1.2) / MgO (1.6) / Ta (20) (all thickness in nm) multilayer. The stack was deposited on a Si/SiO_2 substrate. Both the Ta layers and the $Co_{60}Fe_{20}B_{20}$ layer were deposited by sputtering, and the MgO layer was deposited by electron beam evaporation. During all this fabrication process, there is no vacuum break.

The CF2 and CF3 samples correspond to TTa (5) / Ir (5) / $Co_{60}Fe_{20}B_{20}$ (t) / MgO (1.6) / Ta (20) (all thickness in nm) mutilayers, with $t = 1$ nm and $t = 1.5$ nm, respectively. These samples were deposited similarly to CF1 on a Si/SiO_2 substrate, the metals being deposited by sputtering and the oxide being deposited by electron beam evaporation.

3.2. Magnetic characterization protocol

In order to perform the SQUID-VSM measurements, the protocol developed in [20] was followed. However, some improvements were necessary.

3.2.1 Disabling auto-tracking

Before performing the SQUID-VSM measurement, the sample holder coordinates must be defined to center the sample. To determine the required offset, it's necessary to apply a magnetic field and perform a quick DC scan that shows the detected magnetic moment as a function of position. For samples with high magnetic moment, the maximum moment measured usually appears where the sample is located, and the sample holder offset is defined to center that position. However, if the sample has low magnetic signal, other unwanted contributions, such as impurities, can provide a larger magnetic signal. If that is the case, the program incorrectly defines the offset, and centers the impurity instead of the sample, leading to inaccurate results. Thus, the offset needs to be manually inserted. In the performed out-of-plane measurements, the sample is secured in place between two cylinders that provide a larger signal than the sample. Thus, when the DC scan is performed, the suggested automatic offset always centers one of the cylinders rather than the sample. This suggestion is discarded, and the offset is entered manually.

However, when programming the SQUID-VSM measurements, there is an automatically enabled option which allows the MPMS SQUID to auto-track the sample during the measurements. This option can be useful, as it is constantly centering the sample, providing more accurate magnetic moment measurements. But when dealing with ultrathin films, this option introduces errors. Because the signal of the sample is low compared to the cylinders, the auto-tracking option incorrectly determines the center and incorrectly offsets the sample holder, resulting in measurements with the sample off center. Therefore, it's imperative that this option is disabled.

3.2.2 Stable at each field

Another important improvement was to force stability at each value of magnetic field. Without this requirement, the magnetic field is constantly increasing (decreasing) and the magnetic moment is being measured, meaning that during the time span of the measurement, the magnetic field is changing.

By forcing stability, the magnetic field increases (decreases) and once it's stable at a certain value the magnetic moment is measured, increasing (decreasing) when the measurement is finished. This way, the results are more reliable, as there is no change of magnetic field during the measurement time span.

3.2.3 Measurement parameters

The measurements where the magnetic field is applied out-of-plane were performed with a SQUID-VSM amplitude of 2 mm. The sample holder was made of brass and the sample is attached to the sample holder with Kapton tape. Since we are dealing with samples with a low coercive field, the maximum out-of-plane magnetic field was 500 Oe.

The measurements where the magnetic field is applied in-plane were performed using a SQUID-VSM amplitude of 6 mm and a quartz sample holder. In this case, the maximum magnetic field was 5000 Oe in order to make sure that the sample is fully saturated.

At the beginning of the measurement the temperature is set to 298 K and a magnet reset is performed. The hysteresis cycle is then measured, starting from zero magnetic field.

3.3. Magnetic characterization results

The first step in the analysis of the magnetic hysteresis loops was to remove any unwanted contributions from the obtained signal such as the signal from the substrate, Kapton tape and sample holder. In the case of the in-plane measurements, the main unwanted contributions showed to be diamagnetic while in the out-of-plane measurements they were mostly paramagnetic.

After removing unwanted contributions, the saturation magnetization was determined. The values of saturation magnetization for positive and negative fields were slightly different, so the mean of absolute values was calculated and the data was fitted so that the signal is centered around the magnetization axis. The saturation magnetization determined from the in-plane measurements has shown to be different from the one extracted from the out-of-plane measurements. Theoretically, these should be equal as the the magnetization of a certain sample when it's completely saturated doesn't depend on anisotropy. However, realistically speaking, this result was expected. The SQUID MPMS®3 has an inherent geometrical factor that leads to more accurate results when the sample is magnetized along its anisotropy axis. Therefore, in this work, the more accurate values of saturation magnetization are expected in the out-of-plane measurements.

Once the data is centered, the treatment now depends on the direction of the applied magnetic field, as the goal of each measurement is different. For the in-plane measurements, the goal is to determine the anisotropy field, while for the out-of-plane measurements the goal is to determine the coercive field of the sample.

For the in-plane measurements, the main focus is on the central part of the signal, where the magnetization changes linearly with applied magnetic field. A linear fit of the ascending and descending branches in this area was made and the resulting slopes were averaged in order to fully fit the linear region. The anisotropy field is then determined from the points where the linear fit crosses the saturation magnetization.

For the out-of-plane measurements, the focus is on the step from -M_S to M_S. This step occurs for two values of field which are symmetrical (the coercive field) and to determine them a linear fit is performed on each step (descending and ascending), and the coercive field corresponds to the point where this fit crosses the magnetic field axis. Once again, there is a slight difference between the H_C and $-H_C$ determined values and to correct this error the average is calculated and the data is centered around the origin.

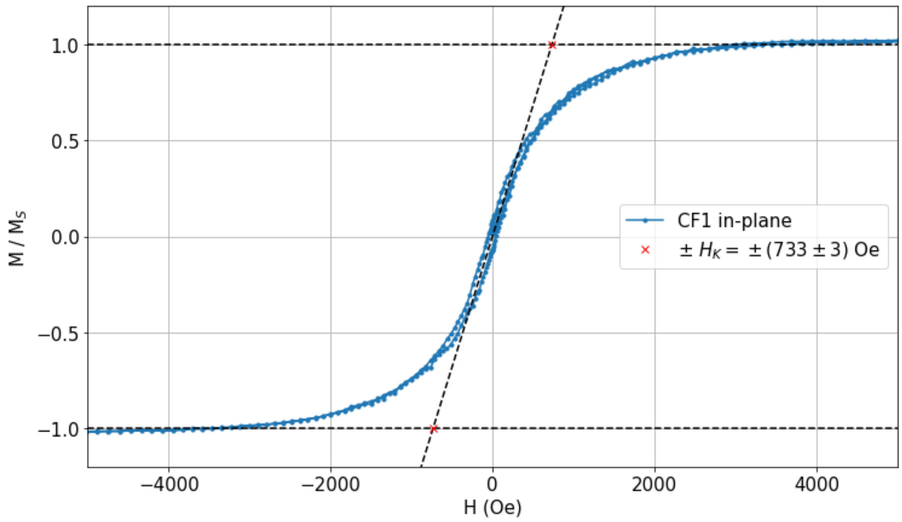

(a) Magnetic field applied along the plane of the sample.

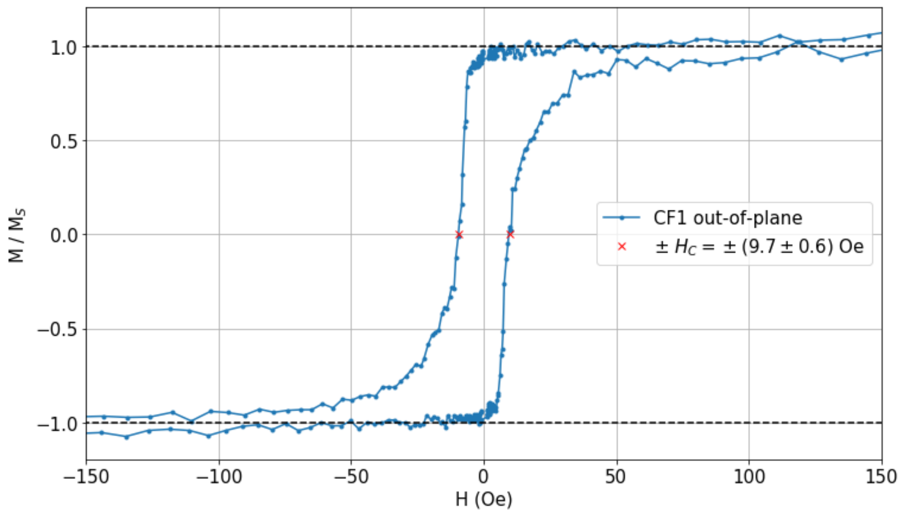

(b) Magnetic field applied perpendicular to the plane of the sample.

Figure 3.2: SQUID-VSM hysteresis cycles of sample CF1.

The CF1 sample has shown perpendicular magnetic anisotropy, as the hysteresis loop along the out-of-plane direction is the one expected for an easy-axis measurement while the in-plane loop shows the linearity expected for a hard axis measurement (figure 3.2). The magnetic properties of the CF1 sample were determined and a magnetization saturation of $M_S = (623 \pm 17)$ emu cm^{-3} was found, which represents a significant deviation of about 38% from the value reported in [4]. This difference between results can arise from the use of different fabrication methods between the two comparing samples, or it can even come as consequence of different amounts of Co, Fe and B in the stack as these are not specified in the referenced article. In addition, both the coercive field and anisotropy field were determined, $H_C = (9.7 \pm 0.6)$ Oe and $H_K = (733 \pm 3)$ Oe, respectively. The coercive field value is in agreement with the literature but the anisotropy field has shown to be significantly smaller than the reported value [4]. This difference can come as a result of the different deposition techniques used to fabricate each sample, once the anisotropy of a certain material is strongly dependent on the the way it was grown.

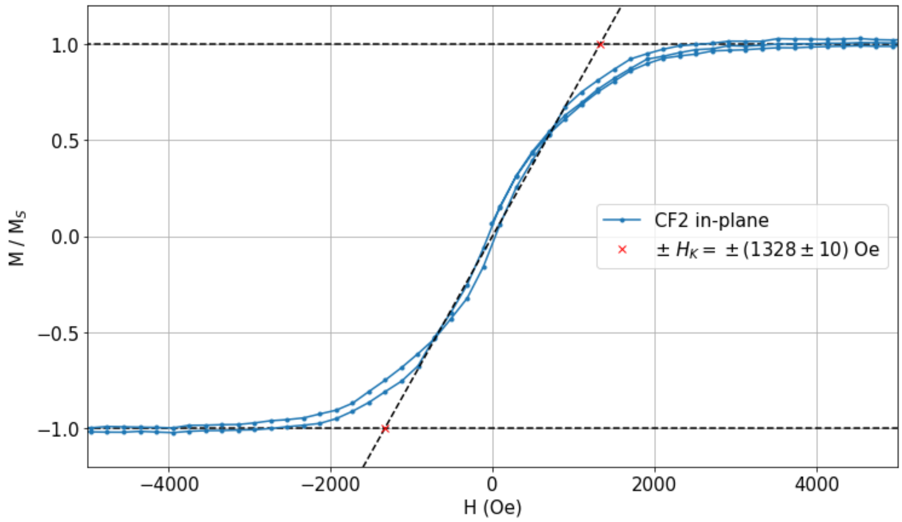

(a) Magnetic field applied along the plane of the sample.

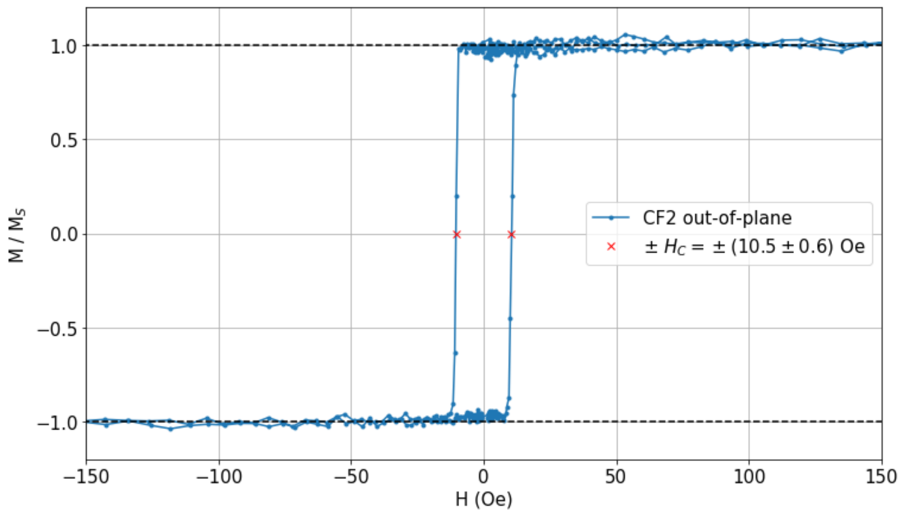

(b) Magnetic field applied perpendicular to the plane of the sample.

Figure 3.3: SQUID-VSM hysteresis cycles of sample CF2.

The CF2 sample also shows perpendicular magnetic anisotropy, due to the shape of both in-plane and out-of-plane loops (figure 3.3). The saturation magnetization in this case is

$M_S = (578 \pm 28)$ emu cm^{-3} which is close to the value obtained for sample CF1. The anisotropy field of sample CF2, $H_K = (1328 \pm 10)$ Oe, has shown to be greater than the anisotropy field obtained for sample CF1, indicating that CF2 has stronger perpendicular magnetic anisotropy. However, the coercive field $H_C = (10.5 \pm 0.6)$ Oe remains roughly the same.

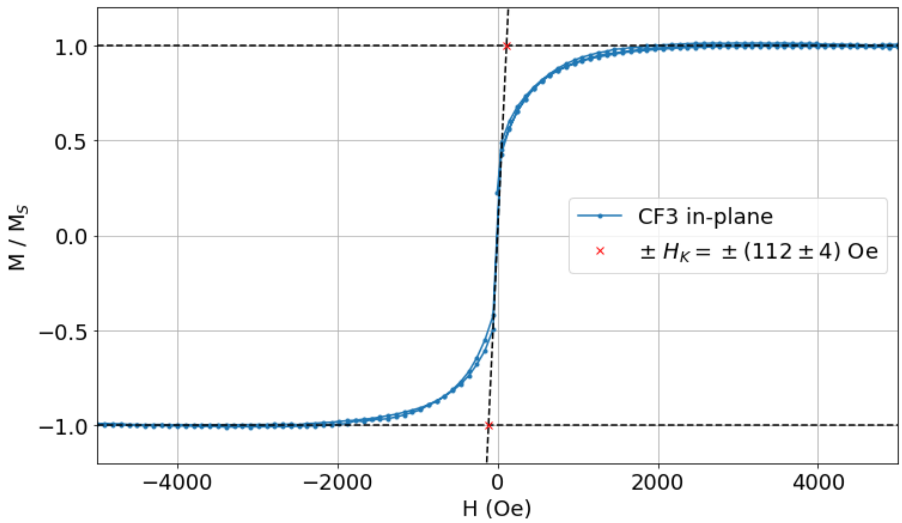

(a) Magnetic field applied along the plane of the sample.

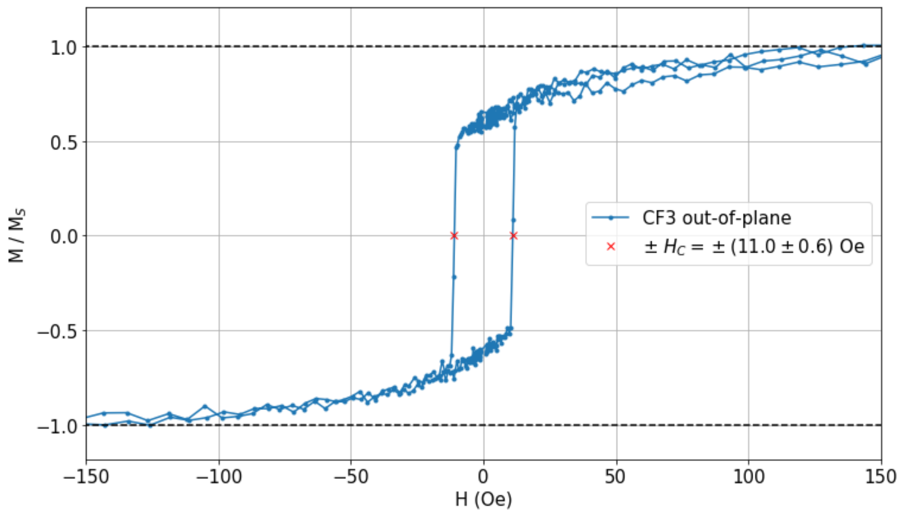

(b) Magnetic field applied perpendicular to the plane of the sample.

Figure 3.4: SQUID-VSM hysteresis cycles of sample CF3.

For the CF3 sample, the out-of-plane hysteresis loop obtained is in agreement with the hysteresis loop expected for a sample subject to a magnetic field slightly deviated from its easy axis (figure 3.4b). Meaning that, in this case, the out-of-plane direction is not the preferential direction for the magnetization. This can come as a result of the CoFeB layer thickness in the CF3 sample. As seen in section 2.1.2, surface anisotropy greatly depends on the thickness of the ferromagnetic layer. In the CF3 sample, the thickness of the CoFeB layer is enough for the anisotropy axis to start to tilt to an in-plane direction. However, the tilt must be small as there are no significant changes in the coercive field value, $H_C = (11.0 \pm 0.6)$ Oe. These results are also verified from the lower value of anisotropy field of CF3, $H_K = (112 \pm 4)$ Oe, compared to CF2. The saturation magnetization has also shown to be significantly different from samples CF1 and CF2, taking the value $M_S = (268 \pm 25)$ emu cm^{-3}.

4. Electrical characterization

4.1. Sample characteristics

In order to develop an electrical measurement protocol, a Ta (10 nm) / CoFeB (1.2 nm) / MgO (1.6 nm) / Ta (20 nm) multilayer was patterned by shadow masking into a Hall cross structure (information on deposition techniques has been provided in section 3.1). It is important to note that this structure was designed exclusively for the protocol implementation, hence its macroscopic dimensions (the width and length of the channels in the Hall devices are 0.5 mm and 2.5 mm, respectively). Therefore, it is not expected to show the spin-orbit torque arising phenomena previously described.

4.2. Physical Property Measurement System (PPMS®)

The electrical characterization of the Hall cross structure was made possible by Quantum Design Physical Property Measurement System (PPMS®). The PPMS is an equipment designed to perform a variety of automated measurements such as electrical transport, thermal and magnetic measurements, providing environments from 1.9 to 400 K and magnetic fields up to 90000 Oe [37].

The base PPMS setup comprises the probe, the dewar, the top-plate assembly, the probe-lifting assembly, a vacuum pump and pumping lines, an electronics cabinet and the Model 600 PPMS Controller [38].

4.2.1 Hardware

4.2.1.1 Dewar and probe

The PPMS probe incorporates temperature-control hardware, a superconducting magnet that provides the magnetic field, a helium-level meter to measure the helium level, the gas lines, the sample puck connectors, and various electrical connections. The magnet is a superconducting solenoid constituted of a niobium–titanium alloy embedded in copper. It is located on the outside of the probe, so it is always immersed in liquid helium. The sample chamber is located inside the probe, between two vacuum tubes, and made of copper, providing a region of uniform temperature. At the bottom of the chamber, there is a 12-pin connector that contacts the bottom of an installed sample puck. The dewar, which contains the liquid-helium bath where the probe is immersed, is made of aluminum and its outer layer has reflective superinsulation in order to minimize helium consumption.

4.2.1.2 Top-plate assembly

The top-plate assembly comprises all the components that seal the sample chamber.

4.2.1.3 Vacuum pump and pumping lines

A direct-drive pump operates continuously to control pressure in the sample chamber and to aid thermal control. Its maintenance is crucial to ensure optimal performance of the PPMS.

4.2.1.4 Sample puck and assorted tools

The PPMS equipment offers two different sample pucks. One universal sample puck and a resistivity sample puck, both constructed of oxygen-free high-conductivity copper and gold-plated to prevent oxidation. The latter, however, presents an interface suitable to easily connect the sample for resistance measurements and, therefore, is compatible with both Electrical Transport Option and DC Resistance Option. Each resistivity sample puck allows to measure the resistance in a four-probe configuration and has connections to three different channels, allowing for simultaneous (two or three, depending on the measurement option) measurements without cross-talking and while maximizing the signal-to-noise ratio.

Another important device is the sample wiring test station as it allows to verify the contact between the sample and the puck. It is particularly useful to determine any unwanted short circuits between contacts before progressing to quality tests and was crucial in the first step of contact quality testing.

To install the puck into the sample chamber, a puck insertion tool is used. This tool grips the puck by a groove in its outer rim and allows to insert the sample into the chamber. Once the puck is connected to the bottom of the sample chamber, we can disengage the puck insertion tool and extract it from the chamber, leaving the puck inside.

4.2.2 Electrical transport measurements in PPMS

This thesis focuses on the electrical transport options provided by the PPMS, as those are the ones suitable for the required electrical characterization. When it comes to electrical transport, the PPMS offers two measurement options depending on the selected excitation mode.

4.2.2.1 Electrical Transport Option (ETO)

The Electrical Transport Option allows for the determination of several electrical transport properties such as resistivity, Hall effect and V-I characteristics. Through a four-probe method, where current flows through the outer two probes and voltage drop is measured across the inner two probes, the ETO allows for accurate resistivity measurements, minimizing the effect of contact resistance.

One important property of ETO is the AC excitation current which shows great interest as it allows to employ lock-in detection techniques. Lock-in techniques can effectively filter out noise, improving the signal-to-noise ratio and accuracy of results. In addition, the use of a high frequency AC current can reduce the dissipated power in the sample and minimize Joule heating effects. Thus, ETO has proved to be a powerful and versatile tool to perform electrical transport measurements with high accuracy and detail.

Lastly, this option allows to simultaneously measure the resistance on up to two channels, providing independent control of each channel and lack of cross-talking.

4.2.2.2 DC Resistance

The DC Resistance (DCR) option is mainly focused on measuring the resistance of a sample as a function of temperature or magnetic field. Similarly to ETO, it can utilize a four-probe method to measure resistance but a two-probe method, where current and voltage are measured using the same pair of contacts, is also available. In this case, a DC excitation current is employed, which can result in a smaller signal-to-noise ratio and less accurate results. In addition, the magnitude of the excitation current should be carefully chosen as to induce a sufficient voltage signal without excessive Joule heating.

This option allows to simultaneously measure the resistance on up to three channels, providing independent control of each channel and lack of cross-talking. It is important to note that, contrary to ETO, the DCR main goal is to determine resistance. Therefore, even though a voltage drop is measured, it is never returned by the system. Instead, the system calculates the resistance from the ratio between the measured voltage drop and excitation current, and returns the determined value.

Here it was shown that ETO is designed for a more thorough and precise study on electrical transport properties while DCR provides simpler and more straightforward resistance measurements. Usually, given both options, the choice between the two depends on the specific requirements of the measurement tasks.

4.2.2.3 Van der Pauw-Hall switching controller

The PPMS offers a Van der Pauw-Hall option that allows to implement the Van der Pauw technique [39]. To implement it, a switching controller is provided and, even though there is no interest to perform a Van der Pauw technique, the ability to switch electronics is attractive.

Thus, The Van der Pauw-Hall switching controller allows to switch electronics in order to perform resistance measurements in a variety of different configurations which was fundamental for this particular work.

In a Hall resistance measurement, a current is injected into one branch of the Hall cross and a Hall voltage is detected in the transversal branch, enabling the determination of the Hall resistance. However, in order to perform a complete characterization of the sample, the ability to switch the current and voltage branches is mandatory, which can not be performed in conventional electrical transport options (ETO or DCR). In fact, the connections established between the sample and the sample puck determine the current branch and the voltage branch: current only flows in the path connected to the I+/I- contacts and voltage can only be measured in the patch connected to the V+/V- contacts.

Hence, by permuting the particular spatial arrangement of the leads which source current and detect the resulting voltage, one can fully electrically characterize the sample without changing the sample setup.

The Van der Pauw-Hall module is theoretically compatible with both ETO and DCR. However, a hardware fault has made it impossible to connect the Van der Pauw-Hall module to the ETO module and, therefore, only the DCR option can be used. Even though the DCR option is simpler, it is expected to be suitable for the required measurements.

4.3. Electrical measurement protocol

4.3.1 Sample mounting

In order to allow for electrical characterization extensive efforts had to be made regarding sample mounting on the sample puck. The process of performing electrical contacts is extremely thorough and time consuming.

Figure 4.1 shows a diagram of the Hall cross sample mounted on a resistivity sample puck in a four-probe configuration.

The gold-plated surface of the sample puck makes electrical contact with the PPMS chamber walls which share a ground with the chamber operations controlling pumps. As these ground can be noisy, it's best to isolate the sample. A suitable material used for this end is cigarette paper, which can be glued to the sample puck with grease. The sample is then tacked to the sample puck with a small amount of grease and the connections are performed. To establish the connections, 0.7 mm copper wires are attached to each sample pad with conducting silver paint. It is crucial to verify that the extremities of the wires are well coated with silver paint in order to well establish the connection to the sample. Once the connections are performed, the silver paint needs to dry. It is common practice to take the device into the oven to speed the drying process. However, since we are dealing with ultrathin films, greatly increasing the temperature could promote intermixing at the interfaces between the layers, compromising the properties of the device. Thus, the device is left to dry at room temperature for at least one day. Once the silver paint is completely dry and the copper wires are well secured to the sample pads, the ends of the wires are welded into the sample puck contacts.

In the present work, the sample was connected to channel 2. For notation simplicity, from now on, each sample pad is assigned a number from 7 to 10 (7/I+, 8/I-, 9/V+, 10/V-), according to the sample wiring test station shown in figure 4.2.

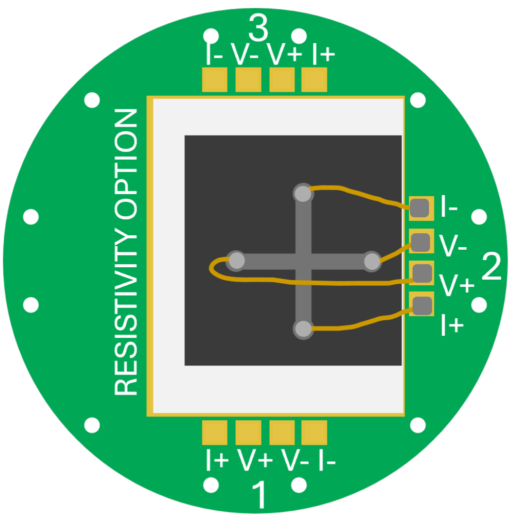

Figure 4.1: Hall cross sample mounted on a resistivity sample puck and respective electric connections (top view).

4.3.2 Electrical contact testing

Before performing any type of electrical transport measurement in the PPMS, it is crucial to verify the quality of the electrical contacts, in particular, it is mandatory to check if we are dealing with ohmic contacts. Therefore, three tests were designed to confirm the quality of the electrical contacts.

4.3.2.1 Direct resistance measurements

The first test consists of directly measuring the resistance between each pair of contacts. In order to perform this test, the sample puck is inserted in the sample wiring test station and banana plugs connected to a digital multimeter in the ohmmeter option are inserted into the jacks. Other than looking for short-circuits between each contact, this test also allows to roughly compare the resistances of the contacts, which are expected to be the same order of magnitude. The test was performed with both positive and negative currents in each combination of contacts.

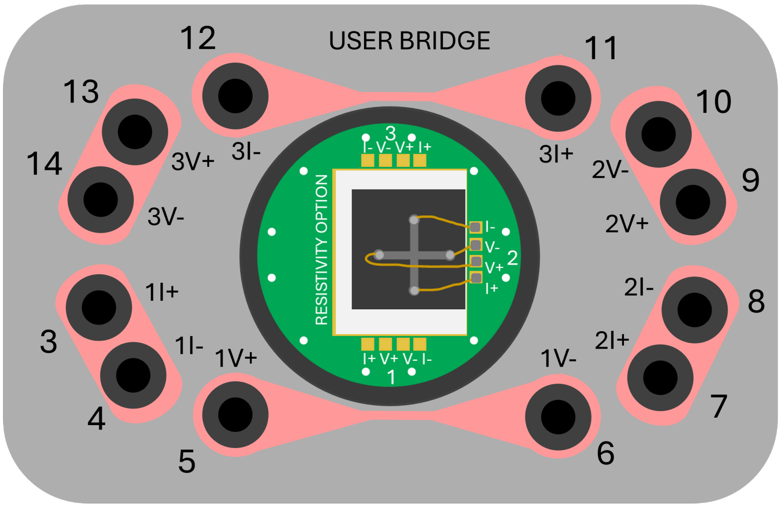

Figure 4.2: Resistivity sample puck mounted on the sample wiring test station (top view). The contacts of each channel (1, 2 and 3) are assigned a number from 6 to 14.

4.3.2.2 Resistance measurement in a two-probe configuration (R2PC)

Next, current is injected into one branch of the Hall cross and the voltage drop is measured, as shown in figure 4.3. For that end, a Keithley's Standard Series 2400 Source Measure Unit was used as it allows to inject current and measure a drop voltage in a two-probe configuration.

Once again, the sample puck was inserted into the sample wiring test station and banana plugs connected to both sourcemeter and test station performed the connections for the desired measurements. The injected current took values in the range of [-1, 1] mA.

(a) R2PCA - Resistance measurement between contacts 7 and 8.

(b) R2PCB - Resistance measurement between contacts 9 and 10.

Figure 4.3: Schematic of the configuration employed to determine resistance using a two-probe method (top view). Current in blue, voltage in orange.

4.3.2.3 Resistance measurement in Hall configuration (RHC)

The last quality test to perform relies on injecting current in one branch of the Hall cross and measuring a transverse voltage drop. In order to perform said examination, two experimental methods were developed.

The first method is similar to test R2PC. The sample puck was inserted into the sample wiring test station and banana plugs connected to both the sourcemeter and the test station performed the required connections for the measurements, now using a four-probe configuration. Current in a range of [-1, 1] mA were injected and the corresponding voltage drop was measured.

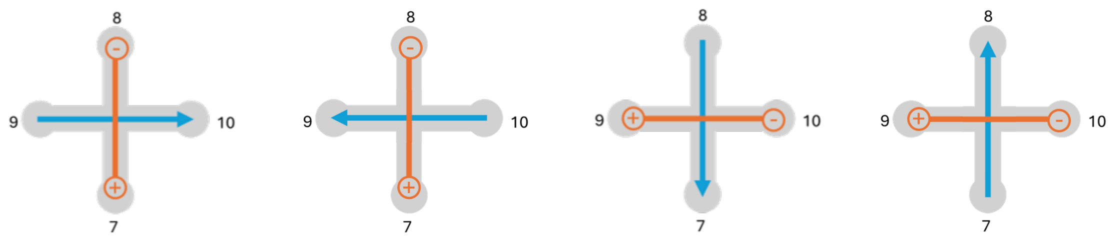

(a) (b) (c) (d)

Figure 4.4: Schematic of the configuration employed to determine resistance using a four-probe method (top view). a,b RHCA - Resistance measurement between contacts 7 and 8 (conventional and inverted polarity, respectively). c,d RHCB - Resistance measurement between contacts 9 and 10 (conventional and inverted polarity, respectively). Current in blue, voltage in orange.

The second is performed with the PPMS DCR option connected to the VdP module. Current values in the range of [-5, 5] mA were injected into the Hall cross but due to the impossibility of acquiring voltage values with the DCR option, values of resistance were converted into voltage, considering the excitation current. The configurations corresponding to this measurements are presented in figure 4.4. Note that with the first method the current provided by the sourcemeter can take negative values as well as positive, therefore only the configurations shown in figures 4.4c and 4.4a are required. In the PPMS DCR option, however, the minimum value of current that can be provided is 0.005 mA, meaning that it can't provide negative values of current. Therefore, it's necessary to switch the current polarity (figures 4.4d and 4.4b) to scan the complete range of desired currents.

4.3.3 Variation of Hall resistance with applied magnetic field

The main electrical transport measurement consists of characterizing the Hall resistance as a function of applied magnetic field. In order to preform this measurement, the PPMS DCR option was used. A current of 5 mA was injected between contacts 7 and 8 and a magnetic field in the range of $H = [-5000, 5000]$ Oe was applied out-of-plane to the sample and the Hall resistance was measured between contacts 9 and 10.

4.4. Results

4.4.1 Electrical contact testing

4.4.1.1 Direct resistance measurements

The resistance values between each contact are shown in table 4.1. As expected, they are of the same order of magnitude, which is important to assure good performance of the device. If one contact was significantly more resistive than the rest, the current would not travel symmetrically through the device, undermining its performance.

Nº of contact	7	8	9	10
7		265 Ω	281 Ω	284 Ω
8	264 Ω		251 Ω	254 Ω
9	280 Ω	251 Ω		281 Ω
10	288 Ω	260 Ω	286 Ω	

Table 4.1: Values of resistance (in Ω) measured between each electrical contact. Uncertainty of $\pm 1\Omega$.

4.4.1.2 Resistance measurement in a two-probe configuration (R2PC)

The collected data were plotted and fitted in order to obtain the resistance between the contacts (figure 4.5). A linear relation is observed between the applied current and the measured voltage, which confirms the ohmic nature of the contacts. Thus, the resistance is given by $R = \frac{V}{I}$, which corresponds to the slope of the fit.

From the fits it was found that the resistance between contacts 7 and 8 is $R_{R2PCA} = (331.5 \pm 0.5)\ \Omega$ and between contacts 9 and 10 is $R_{R2PCB} = (426.9 \pm 0.5)\ \Omega$. It is clear that the path between contacts 9 and 10 is more resistive. However, they have the same order of magnitude meaning this difference is not relevant.

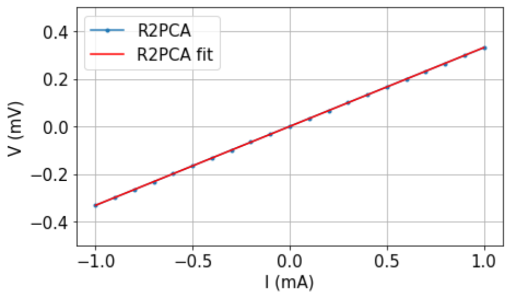

(a) R2PCA - Resistance measurement between contacts 7 and 8.

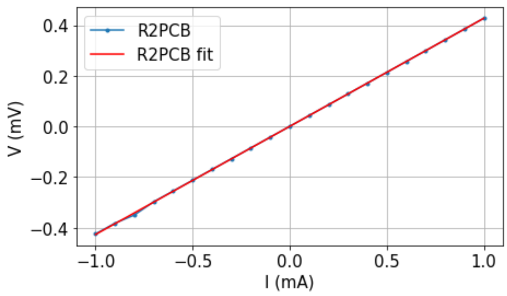

(b) R2PCB - Resistance measurement between contacts 9 and 10.

Figure 4.5: V-I curves obtained in a two-probe configuration.

4.4.1.3 Transverse voltage measurement in Hall configuration (RHC)

First, we will discuss the results obtained with the sourcemeter method. Theoretically, considering that the current is confined to the channel where it's injected, and in the absence of magnetic field, no transverse voltage was expected. However, the results show that a transverse voltage arises and changes linearly with the applied current. In fact, experimentally, this result was expected and can arise from several causes: slight misalignment of contacts, causing asymmetries in the device, non-uniform current distribution or even defects and inhomogeneities in the material. The negative slope of the data has no real physical meaning, translating only the direction of the unwanted asymmetries. By converting this transverse voltage into a transverse resistance like quantity (which also has no physical meaning), $R_{RHCA} = (-0.2 \pm 0.3)\ \Omega$ and $R_{RHCB} = (-0.2 \pm 0.3)\ \Omega$, it is shown that this transverse voltage can be disregarded.

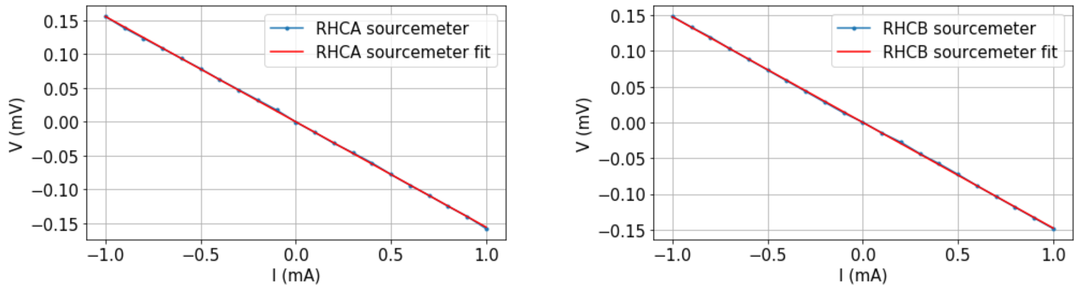

(a) RHCA - Resistance measurement between contacts 7 and 8.

(b) RHCB - Resistance measurement between contacts 9 and 10.

Figure 4.6: V-I curves obtained in a Hall configuration with the sourcemeter.

The results obtained with the PPMS were analogous to the ones previously shown. A transverse voltage was found to change linearly with the excitation current and the calculated transverse resistance like values were the same as previously mentioned, confirming the accuracy of the acquired data.

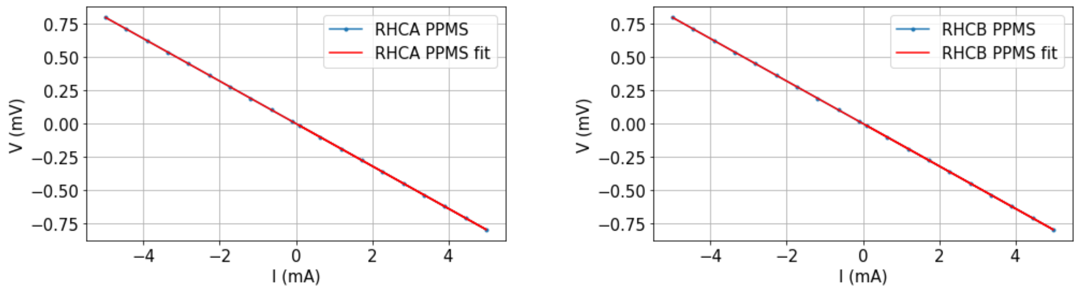

(a) RHCA - Resistance measurement between contacts 7 and 8.

(b) RHCB - Resistance measurement between contacts 9 and 10.

Figure 4.7: V-I curves obtained in a Hall configuration with the PPMS.

4.4.2 Variation of Hall resistance to out-of-plane magnetic field

The acquired data showed a linear relation between the measured resistance and the applied magnetic field, indicating the existence of ordinary Hall effect. At zero magnetic field, no Hall voltage is expected, but a non-zero resistance arises from the measurement due to unwanted contributions such as the resistance measured in test RHC and electrical drifts of the system. These contributions were removed in order to isolate the contribution from the Hall effect.

The current is injected through the electrical contacts and travels through the top layer of Ta. Below Ta, there is MgO which has insulating properties. Therefore, we are most likely observing the ordinary Hall effect in the top layer of Ta, measuring a Hall coefficient

$R_H = (-1.034 \pm 0.005)\ \mu\Omega$/Oe. However, this value is significantly larger than the typically expected for Ta thin films which can indicate that ordinary Hall effect in Ta might be amplified by the relatively high current density in the cross-sectional area of the channel.

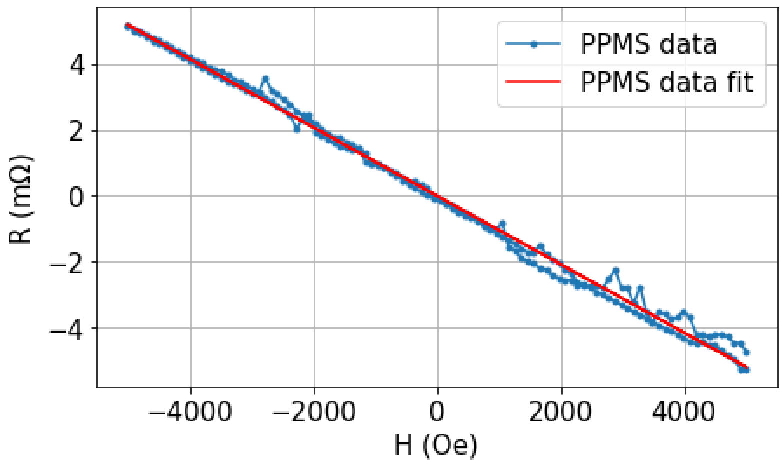

Figure 4.8: R-H curve obtained in a Hall configuration with the PPMS. Measurement performed with an excitation current of 5 mA.

5. Conclusion

5.1. Results summary

	M_S (emu cm^{-3})	H_C (Oe)	H_K (Oe)
CF1	623 ± 17	9.7 ± 0.6	733 ± 3
CF2	578 ± 28	10.5 ± 0.6	1328 ± 10
CF3	268 ± 25	11.0 ± 0.6	112 ± 4

Table 5.1: Magnetic characterization results.

The present work provides improvements on the established protocol for measuring the magnetic properties of ultrathin films with perpendicular magnetic anisotropy in the MPMS SQUID VSM, as well as establishes a protocol to perform Hall resistance measurements in the PPMS, regarding the sample mounting, electric contact testing and resistance measurements in Hall configuration with magnetic field applied perpendicular to the plane of the sample.

The performed electrical characterization allowed to measure a Hall coefficient of $R_H = -(1.034 \pm 0.005) \mu\Omega$/Oe which most likely comes from the top Ta layer. However, the measurement protocol is suitable for measuring resistance in Hall configuration for other Hall structures, meaning that given a HM/CoFeB/MgO/HM multilayer with adequate dimensions, it is also suitable for measuring the anomalous Hall resistance.

Regarding the magnetic characterization protocol, two important improvements were made: forcing stability of magnetic field at each point and disabling the auto-tracking of the sample. This protocol allowed to determine the magnetic properties of three continuous films, and the results are shown in table 5.1. From these results it was possible to conclude that increasing the thickness of CoFeB to 1.5 nm leads to the tilt of the anisotropy axis, making sample CF3 not suitable for spin-orbit torque enabled sensing. It was also verified that the addition of iridium doesn't cause significant influence on the coercivity of the hysteresis loops. It can, however increase the perpendicular magnetic anisotropy energy of the device.

A lot of work still needs to be done regarding the topic, but the foundations are set for electrical and magnetic characterization of ultrathin films, which opens the pathway for upcoming scientific development.

5.2. Outlook

Having set the foundations for electrical and magnetic characterization of ultrathin films for magnetic sensing, it would now be interesting to employ them into characterizing a spin-orbit torque enabled sensor similar to the one reported in [4]. Thus, a Ta (10 nm) / CoFeB (1.2 nm) / MgO (1.6 nm) / Ta (20 nm) multilayer was patterned by shadow masking into Hall cross structures aiming for future characterization. The mask was designed so that the width and length of the Hall cross channels were 5 μm and 200 μm, respectively, and the dimensions of the device pads were 1000 μm × 1000 μm. The dimensions of the pocket size are 1 cm $\times$ 1 cm so the mask can comprise five Hall structures in this area, as shown in figure 5.1.

The width of the Hall cross was determined considering the current limitations of the PPMS DCR option connected to the VdP module and the required current density reported in [4] to close the hysteresis loop. The maximum width of the Hall channel given these values would be around 7 μm. Therefore, a width of 5 μm was chosen. The length was chosen to replicate the device reported in [4]. The size of the pads was selected considering the thickness of the copper wires that perform the electric connections, making sure that they are big enough to perform the connection with silver paint.

Thus, the next step would be to magnetically and electrically characterize this sample, following the developed protocols, in hopes of replicating the results obtained in [4].

Alongside this characterization, the exploration of using different heavy metals should continue, as it seems to be the path for larger range 3D magnetic sensor consisting of a single element.

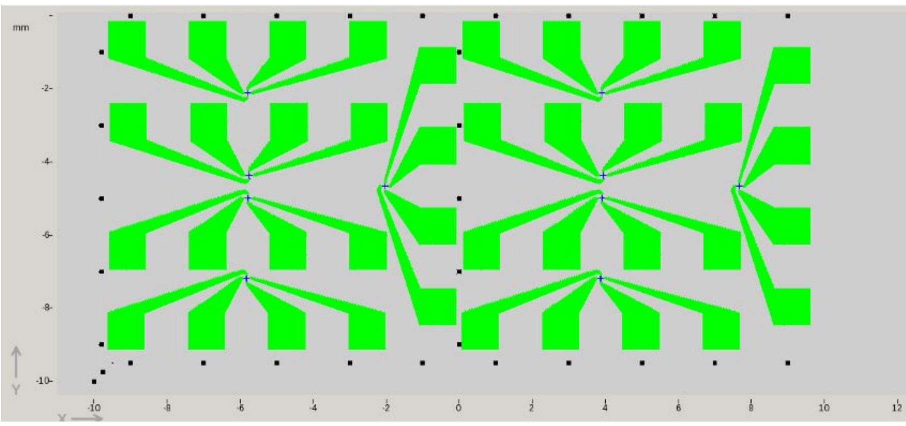

Figure 5.1: Mask layout of two samples, each with five Hall crosses.

5.3. Final thoughts

The main goal of this work is fulfilled: it sets the foundations for electrical and magnetic characterization of ultrathin films for magnetic sensing.

Regarding, in particular, spin-orbit torque enabled magnetic sensors, this thesis paves the way to improve their understanding and characterization. It provides well established measurement protocols for electrical and magnetic characterization, presents ultrathin film engineering results regarding suitable materials and thickness and delivers the devising of a microdevice magnetic sensor, all important tools for exploring new issues and opening the pathway for upcoming scientific development.

References

[1] S. Marshall, “Vehicle detection using a magnetic field sensor,” *IEEE Transactions on Vehicular Technology*, vol. 27, no. 2, pp. 65–68, 1978. [Cited on page 1.]

[2] J. Lenz and S. Edelstein, “Magnetic sensors and their applications,” *IEEE Sensors Journal*, vol. 6, no. 3, pp. 631–649, 2006.

[3] K. Tsukada, M. Hayashi, Y. Nakamura, K. Sakai, and T. Kiwa, “Small eddy current testing sensor probe using a tunneling magnetoresistance sensor to detect cracks in steel structures,” *IEEE Transactions on Magnetics*, vol. PP, pp. 1–5, 06 2018.

[4] R. Li, S. Zhang, S. Luo, Z. Guo, Y. Xu, M. Song, Q. Zou, L. Xi, X. Yang, J. Hong, and L. You, “A spin–orbit torque device for sensing three-dimensional magnetic fields,” *Nature Electronics*, vol. 4, pp. 1–6, 03 2021. [Cited on pages viii, 1, 2, 3, 16, 17, 18, 23, and 38.]

[5] Z. Guo, R. Li, S. Zhang, Y. Tian, J. Hong, and L. You, “A three-dimensional magnetic field sensor based on a single spin–orbit-torque device via domain nucleation,” *Applied Physics Letters*, vol. 120, p. 232404, 06 2022. [Cited on pages 1, 2, 16, and 17.]

[6] J. M. D. Coey, *Magnetism and Magnetic Materials*. Cambridge University Press, 2010. [Cited on pages 1, 5, 6, 7, 8, 9, and 13.]

[7] B. Dieny, I. L. Prejbeanu, K. Garello, P. Gambardella, P. Freitas, R. Lehndorff, W. Raberg, U. Ebels, S. O. Demokritov, J. Akerman, A. Deac, P. Pirro, C. Adelmann, A. Anane, A. V. Chumak, A. Hirohata, S. Mangin, S. O. Valenzuela, M. C. Onbaşlı, M. d’Aquino, G. Prenat, G. Finocchio, L. Lopez-Diaz, R. Chantrell, O. Chubykalo-Fesenko, and P. Bortolotti, “Opportunities and challenges for spintronics in the microelectronics industry,” *Nature Electronics*, vol. 3, no. 8, pp. 446–459, Aug. 2020, number: 8 Publisher: Nature Publishing Group. [Online]. Available: https://www.nature.com/articles/s41928-020-0461-5 [Cited on page 1.]

[8] D. Leitao, A. Silva, E. Paz, R. Ferreira, S. Cardoso, and P. Freitas, “Magnetoresistive nanosensors: Controlling magnetism at the nanoscale,” *Nanotechnology*, vol. 27, p. 045501, 12 2015. [Cited on page 1.]

[9] D. J. Adelerhof and W. Geven, “New position detectors based on amr sensors,” *Sensors and Actuators A: Physical*, vol. 85, no. 1, pp. 48–53, 2000. [Online]. Available: https://www.sciencedirect.com/science/article/pii/S0924424700003411 [Cited on page 1.]

[10] N. Pérez, M. Melzer, D. Makarov, O. Ueberschär, R. Ecke, S. Schulz, and O. Schmidt, “High-performance giant magnetoresistive sensorics on flexible si membranes,” *Applied Physics Letters*, vol. 106, p. 153501, 04 2015. [Cited on page 1.]

[11] N. Pertsev, “Magnetic tunnel junction on a magnetostrictive substrate: An ultrasensitive magnetic-field sensor,” *Applied Physics Letters*, vol. 109, p. 132406, 09 2016. [Cited on page 1.]

[12] H. Ohno, M. Stiles, and B. Dieny, “Spintronics,” *Proceedings of the IEEE*, vol. 104, no. 10, pp. 1782–1786, Oct. 2016, publisher Copyright: © 1963-2012 IEEE. [Cited on page 1.]

[13] C. Becker, B. Bao, D. Karnaushenko, V. Bandari, B. Rivkin, Z. Li, M. Faghih, D. Karnaushenko, and O. Schmidt, “A new dimension for magnetosensitive e-skins: active matrix integrated micro-origami sensor arrays,” *Nature Communications*, vol. 13, p. 2121, 04 2022. [Cited on page 1.]

[14] R. Popovic, “The vertical hall-effect device,” *IEEE Electron Device Letters*, vol. 5, no. 9, pp. 357–358, 1984. [Cited on page 1.]

[15] V. S. Luong, Y.-H. Su, C.-C. Lu, J.-T. Jeng, J.-H. Hsu, M.-H. Liao, J. C. Wu, M.-H. Lai, and C.-R. Chang, “Planarization, fabrication, and characterization of three-dimensional magnetic field sensors,” *IEEE Transactions on Nanotechnology*, vol. PP, pp. 1–1, 01 2017. [Cited on page 1.]

[16] Y. Wu, Y. Xu, Z. Luo, Y. Yang, H. Xie, Q. Zhang, and X. Zhang, “Charge–spin interconversion and its applications in magnetic sensing,” *Journal of Applied Physics*, vol. 129, p. 060902, 02 2021. [Cited on pages 1, 2, and 11.]

[17] X. Han, X. Wang, C. Wan, G. Yu, and X. Lv, “Spin-orbit torques: Materials, physics, and devices,” *Applied Physics Letters*, vol. 118, p. 120502, 03 2021. [Cited on pages 1, 2, 11, and 12.]

[18] N. Nagaosa, J. Sinova, S. Onoda, A. MacDonald, and N. Ong, "Anomalous hall effect," *Reviews of Modern Physics*, vol. 82, no. 2, pp. 1539–1592, May 2010. [Cited on pages 2, 13, and 14.]

[19] S. Koraltan, R. Gupta, R. P. Pradeep, F. Kammerbauer, I. Kononenko, K. Prügl, M. Kirsch, B. Aichner, S. Helbig, F. Bruckner, C. Abert, A. O. Mandru, A. Satz, G. Jakob, H. J. Hug, M. Kläui, and D. Suess, "Skyrmionic device for three dimensional magnetic field sensing enabled by spin-orbit torques," 2024. [Online]. Available: https://arxiv.org/abs/2403.16725 [Cited on page 2.]

[20] J. Moutinho, "Exploring spin-orbit torque multilayers: Characterisation and modelling of cofeb films towards magnetic sensors," Master's thesis, University of Porto, 2024. [Cited on pages 2, 10, and 19.]

[21] W. Skowroński, T. Nozaki, Y. Shiota, S. Tamaru, K. Yakushiji, H. Kubota, A. Fukushima, S. Yuasa, and Y. Suzuki, "Perpendicular magnetic anisotropy of ir/-cofeb/mgo trilayer system tuned by electric fields," *Applied Physics Express*, vol. 8, p. 053003, 04 2015. [Cited on page 3.]

[22] E. Stoner and E. Wohlfarth, "A mechanism of magnetic hysteresis in heterogeneous alloys," *IEEE Transactions on Magnetics*, vol. 27, no. 4, pp. 3475–3518, 1991. [Cited on page 4.]

[23] K. Krishnan, *Fundamentals and Applications of Magnetic Materials*. Oxford University Press, 2016. [Online]. Available: https://books.google.pt/books?id=QBo1DQAAQBAJ [Cited on pages 4 and 5.]

[24] S. Blundell, *Magnetism in Condensed Matter*, reprint ed., ser. Oxford Master Series in Condensed Matter Physics. Oxford: Oxford Univ. Press, 2014, no. 4. [Cited on page 9.]

[25] J. D. Jackson, *Classical electrodynamics*, 3rd ed. New York, NY: Wiley, 1999. [Online]. Available: http://cdsweb.cern.ch/record/490457 [Cited on pages 9 and 10.]

[26] A. Soumyanarayanan, N. Reyren, F. Albert, and C. Panagopoulos, "Emergent phenomena induced by spin-orbit coupling at surfaces and interfaces," *Nature*, vol. 539, pp. 509–517, 11 2016. [Cited on page 11.]

[27] A. Nasseri, B. Sarma, G. Durin, and C. Serpico, "Analytical modelling of magnetic dw motion," *Physics Procedia*, vol. 75, pp. 974–985, 12 2015. [Cited on page 12.]

[28] M. Jiang, H. Asahara, S. Sato, S. Ohya, and M. Tanaka, “Suppression of the field-like torque for efficient magnetization switching in a spin–orbit ferromagnet,” *Nature Electronics*, vol. 3, pp. 1–6, 12 2020. [Cited on page 13.]

[29] C. Abert, H. Sepehri-Amin, F. Bruckner, C. Vogler, M. Hayashi, and D. Suess, “Fieldlike and dampinglike spin-transfer torque in magnetic multilayers,” *Phys. Rev. Appl.*, vol. 7, p. 054007, May 2017. [Online]. Available: https://link.aps.org/doi/10.1103/PhysRevApplied.7.054007 [Cited on page 13.]

[30] A. W. Smith and R. W. Sears, “The hall effect in permalloy,” *Phys. Rev.*, vol. 34, pp. 1466–1473, Dec 1929. [Online]. Available: https://link.aps.org/doi/10.1103/PhysRev.34.1466 [Cited on page 13.]

[31] E. M. Pugh, “Hall effect and the magnetic properties of some ferromagnetic materials,” *Phys. Rev.*, vol. 36, pp. 1503–1511, Nov 1930. [Online]. Available: https://link.aps.org/doi/10.1103/PhysRev.36.1503 [Cited on page 13.]

[32] E. M. Pugh and T. W. Lippert, “Hall e.m.f. and intensity of magnetization,” *Phys. Rev.*, vol. 42, pp. 709–713, Dec 1932. [Online]. Available: https://link.aps.org/doi/10.1103/PhysRev.42.709 [Cited on page 13.]

[33] R. Karplus and J. M. Luttinger, “Hall effect in ferromagnetics,” *Phys. Rev.*, vol. 95, pp. 1154–1160, Sep 1954. [Online]. Available: https://link.aps.org/doi/10.1103/PhysRev.95.1154 [Cited on page 14.]

[34] J. Smit, “The spontaneous hall effect in ferromagnetics i,” *Physica*, vol. 21, no. 6, pp. 877–887, 1955. [Online]. Available: https://www.sciencedirect.com/science/article/pii/S0031891455925969 [Cited on page 14.]

[35] S. Zhang, S. Luo, N. Xu, Q. Zou, M. Song, J. Yun, Q. Luo, Z. Guo, R. Li, W. Tian, X. Li, H. Zhou, H. Chen, Y. Zhang, X. Yang, W. Jiang, K. Shen, J. Hong, Z. Yuan, L. Xi, K. Xia, S. Salahuddin, B. Dieny, and L. You, “A spin–orbit-torque memristive device,” *Advanced Electronic Materials*, vol. 5, no. 4, p. 1800782, 2019. [Online]. Available: https://onlinelibrary.wiley.com/doi/abs/10.1002/aelm.201800782 [Cited on page 15.]

[36] L. Liu, O. J. Lee, T. J. Gudmundsen, D. C. Ralph, and R. A. Buhrman, “Current-induced switching of perpendicularly magnetized magnetic layers using spin torque from the spin hall effect,” *Phys. Rev. Lett.*, vol. 109, p. 096602, Aug

2012. [Online]. Available: https://link.aps.org/doi/10.1103/PhysRevLett.109.096602 [Cited on page 16.]

[37] Q. Design, *PPMS Platform Measurement Options*, Quantum Design Inc., technical Manual. [Cited on page 26.]

[38] ——, *Physical Property Measurement System: Hardware Manual*, Quantum Design Inc., technical Manual. [Cited on page 26.]

[39] ——, *Van der Pauw - Hall Option: User's Manual*, Quantum Design Inc., technical Manual. [Cited on page 29.]